

THE VMC SURVEY. XIX. CLASSICAL CEPHEIDS IN THE SMALL MAGELLANIC CLOUD

V. RIPEPI¹

INAF-Osservatorio Astronomico di Capodimonte, via Moiariello 16, 80131, Naples, Italy

M. MARCONI¹

INAF-Osservatorio Astronomico di Capodimonte, via Moiariello 16, 80131, Naples, Italy

M. I. MORETTI²

IAASARS, National Observatory of Athens, 15236 Penteli, Greece

G. CLEMENTINI³

INAF-Osservatorio Astronomico di Bologna, via Ranzani , 40127, Bologna, Italy

M.-R. L. CIONI^{4,5,6}

Universität Potsdam, Institut für Physik und Astronomie, Karl-Liebknecht-Str. 24/25, 14476 Potsdam, Germany
Leibniz-Institut für Astrophysik Potsdam, An der Sternwarte 16, 14482 Potsdam Germany
Centre for Astrophysics Research, School of Physics, Astronomy and Mathematics, University of Hertfordshire, College Lane, Hatfield AL10 9AB, UK

R. DE GRIJS^{7,8}

Kavli Institute for Astronomy & Astrophysics and Department of Astronomy, Peking University, Yi He Yuan Lu 5, Hai Dian District, Beijing 100871, China
International Space Science Institute–Beijing, 1 Nanertiao, Zhongguancun, Hai Dian District, Beijing 100190, China

J. P. EMERSON⁹

School of Physics & Astronomy, Queen Mary University of London, Mile End Road, London E1 4NS, United Kingdom

M. A. T. GROENEWEGER¹⁰

Koninklijke Sterrenwacht van België, Ringlaan 3, 1180, Brussel, Belgium

V. D. IVANOV¹¹

European Southern Observatory, Karl-Schwarzschild-Strasse 2, 85748 Garching bei München, Germany

A. E. PIATTI^{12,13}

Observatorio Astronómico, Universidad Nacional de Córdoba, Laprida 854, 5000, Córdoba, Argentina
Consejo Nacional de Investigaciones Científicas y Técnicas, Av. Rivadavia 1917, C1033AAJ, Buenos Aires, Argentina
Draft version July 17, 2021

ABSTRACT

The *VISTA near-infrared YJK_s* survey of the *Magellanic System* (VMC) is collecting deep *K_s*-band time-series photometry of pulsating variable stars hosted by the two Magellanic Clouds and their connecting Bridge. In this paper, we present *Y*, *J*, *K_s* light curves for a sample of 4172 Small Magellanic Cloud (SMC) Classical Cepheids (CCs). These data, complemented with literature *V* values, allowed us to construct a variety of period-luminosity (*PL*), period-luminosity-color (*PLC*), and period-Wesenheit (*PW*) relationships, valid for Fundamental (F), First Overtone (FO) and Second Overtone (SO) pulsators. The relations involving *V*, *J*, *K_s* bands are in agreement with their counterparts in the literature. As for the *Y* band, to our knowledge we present the first CC *PL*, *PW*, and *PLC* relations ever derived using this filter. We also present the first near-infrared *PL*, *PW*, and *PLC* relations for SO pulsators to date. We used *PW(V, K_s)* to estimate the relative SMC–LMC distance and, in turn, the absolute distance to the SMC. For the former quantity we find a value of $\Delta\mu = 0.55 \pm 0.04$ mag, in rather good agreement with other evaluations based on CCs, but significantly larger than the results obtained from older population II distance indicators. This discrepancy might be due to the different geometric distributions of young and old tracers in both Clouds. As for the absolute distance to the SMC, our best estimates are $\mu_{\text{SMC}} = 19.01 \pm 0.05$ mag and $\mu_{\text{SMC}} = 19.04 \pm 0.06$ mag, based on two distance measurements to the LMC, which rely on accurate CC and eclipsing Cepheid binary data, respectively.

Keywords: stars: variables: Cepheids; stars: oscillations; galaxies: Magellanic Clouds; cosmology: distance scale

1. INTRODUCTION

The Magellanic Clouds (MCs) are fundamental touchstones in the context of stellar populations and galactic evolution studies (see, e.g., Harris & Zaritsky 2004, 2009; Ripepi et al. 2014a). Indeed, they are relatively close ($D_{\odot} \sim 50 - 60$ kpc Westerlund 1997; Udalski et al. 1999), they are rich in stars of different ages, and their morphologies have been significantly affected by their dynamical interaction. In effect, there are clear signatures that the Small Magellanic Cloud (SMC), a gas-rich, dwarf irregular galaxy, is interacting with its neighbours, the Large Magellanic Cloud (LMC) and the Milky Way (MW). In particular, the MCs are connected by a Bridge dominated by HI gas but which also contains a significant stellar content (e.g. Irwin et al. 1985; Harris 2007). Like the Magellanic Stream, the Bridge may be the signature of the MCs' mutual gravitational effects and/or the impact of the MW (e.g. Putman et al. 1998; Hammer et al. 2015). In addition, the SMC Wing, the part of the SMC main body extending asymmetrically towards the LMC (Shapley 1940), could be the result of tidal interaction(s). Moreover, the bar of the SMC, traced by the galaxy's young populations, appears highly asymmetric and elongated, with its northeastern portion closer to us than its southwestern part (e.g. Welch et al. 1987; Haschke et al. 2012; Rubele et al. 2015; Scowcroft et al. 2016). In general, the morphology of the SMC appears to depend on the age of the stellar population used as a probe (see, e.g. Cioni et al. 2000a; Zaritsky et al. 2000; Dobbie et al. 2014; Deb et al. 2015, and references therein). The study of the structure of the SMC is further complicated by the presence of a considerable line-of-sight depth variation in the galaxy. Despite several studies, it appears that the precise extent of the line-of-sight depth and the three-dimensional (3D) geometry

of the SMC are still rather uncertain (see, e.g. de Grijs et al. 2014, for a review). In fact, a comparison of the results in the recent literature adopting different methods, namely horizontal-branch stars, RR Lyrae and/or Classical Cepheid (CC) variables, red-clump stars, full star-formation-history (SFH) reconstruction, star clusters, etc., showed good qualitative agreement, but significant discrepancies in the quantitative description of the geometry of the SMC remain (see, e.g. Hatzidimitriou & Hawkins 1989; Stanimirović et al. 2004; Glatt et al. 2008; Nidever et al. 2013; Deb et al. 2015; Subramanian & Subramanian 2015; Rubele et al. 2015, and references therein).

CC variables are at the base of the absolute calibration of the extragalactic distance scale (see, e.g. Freedman et al. 2001; Marconi et al. 2005; Riess et al. 2011; Fiorentino et al. 2013, and references therein) through their well known Period–Luminosity (*PL*), Period–Luminosity–Color (*PLC*), and Period–Wesenheit (*PW*) relationships.

The CC *PL* relations have been demonstrated, by several authors, to show a nonnegligible dependence on both metallicity (see, e.g. Caputo et al. 2000; Romaniello et al. 2008; Bono et al. 2010, and references therein) and helium content (see Fiorentino et al. 2002; Marconi et al. 2005; Carini et al. 2014), and to exhibit a nonlinear behavior towards the longest periods (see, e.g. Caputo et al. 2000; Ngeow et al. 2008; Marconi 2009, and references therein). Both effects, combined with the intrinsic dispersion due to the finite width of the instability strip, are significantly reduced at near-infrared (NIR) wavelengths (Bono et al. 1999; Caputo et al. 2000; Marconi et al. 2005, 2010).

The *PLC* relations hold for each individual pulsator, since they result from the combination of the period–density, the Stefan–Boltzmann, and the Mass–Luminosity relations (see, e.g. Bono et al. 1999, for details), but they are affected by reddening and metallicity uncertainties. On the other hand, the *PW* relations are reddening-free by definition (e.g. Madore 1982; Caputo et al. 2000) and include a color term that accounts at least in part for the finite width of the instability strip. Moreover, they are less dependent on chemical composition than the *PL* relations. Furthermore, pulsation amplitudes are much smaller in the NIR than in the optical bands, and thus accurate mean magnitudes can be derived from a smaller number of phase points along the pulsation cycle with respect to the optical bands.

The *VISTA*¹⁴ near-infrared *YJK_s* survey of the Magellanic Clouds system (VMC; Cioni et al. 2011) aims at obtaining deep NIR photometric data in the *Y*, *J*, and *K_s* filters over a wide area covering the entire Magellanic system. VMC is a European Southern Observatory (ESO) public survey that is carried out with VIRCAM (VISTA InfraRed Camera) (Dalton et al. 2006) on the ESO/VISTA telescope (Emerson et al. 2006). The main goals of the survey are to reconstruct the SFH and its

Electronic address: ripepi@oacn.inaf.it

¹ INAF-Osservatorio Astronomico di Capodimonte, via Moiariello 16, 80131, Naples, Italy

² IAASARS, National Observatory of Athens, 15236 Penteli, Greece

³ INAF-Osservatorio Astronomico di Bologna, via Ranzani, 1, 40127, Bologna, Italy

⁴ Universität Potsdam, Institut für Physik und Astronomie, Karl-Liebknecht-Str. 24/25, 14476 Potsdam, Germany

⁵ Leibniz-Institut für Astrophysik Potsdam, An der Sternwarte 16, 14482 Potsdam Germany

⁶ University of Hertfordshire, Physics Astronomy and Mathematics, College Lane, Hatfield AL10 9AB, United Kingdom

⁷ Kavli Institute for Astronomy & Astrophysics and Department of Astronomy, Peking University, Yi He Yuan Lu 5, Hai Dian District, Beijing 100871, China

⁸ International Space Science Institute–Beijing, 1 Nanertiao, Zhongguancun, Hai Dian District, Beijing 100190, China

⁹ School of Physics & Astronomy, Queen Mary University of London, Mile End Road, London E1 4NS, United Kingdom

¹⁰ Koninklijke Sterrenwacht van België, Ringlaan 3, 1180, Brussel, Belgium

¹¹ European Southern Observatory, Karl-Schwarzschild-Strasse 2, 85748 Garching bei München, Germany

¹² Observatorio Astronómico, Universidad Nacional de Córdoba, Laprida 854, 5000, Córdoba, Argentina

¹³ Consejo Nacional de Investigaciones Científicas y Técnicas, Av. Rivadavia 1917, C1033AAJ, Buenos Aires, Argentina

¹⁴ Visible and Infrared Survey Telescope for Astronomy

spatial variation, as well as infer an accurate 3D map of the entire Magellanic system. The properties of pulsating stars observed by the VMC in the LMC and used as tracers of three different stellar populations, namely CCs (younger than a few hundred Myr), RR Lyrae and Type II Cepheid stars (older than 9–10 Gyr), and Anomalous Cepheids (traditionally associated with an intermediate-age population of a few Gyr¹⁵), have been discussed in recent papers by our team (Ripepi et al. 2012a,b; Moretti et al. 2014; Ripepi et al. 2014b; Muraveva et al. 2015; Ripepi et al. 2015). In these papers, we provided relevant results on the calibration of the distance scale for all these important standard candles.

The scope of this paper is to present the results for the CCs in the SMC after four years of VMC observations. The SMC is known to host more than 4500 CCs, according to the OGLE III (Soszyński et al. 2010) and EROS 2 (Tisserand et al. 2007; Kim et al. 2014) surveys. The large number of these pulsators, combined with their characteristic narrow intrinsic PL , PLC , and PW relationships in the NIR, make them perfect tracers to unveil the complex structure of the SMC. Indeed, as outlined above, the use of NIR relations has several advantages with respect to the optical bands. Thus, the data presented in this paper will allow us to study in more detail compared with past studies the 3D geometry of the galaxy. The results of that analysis will be presented in a forthcoming paper.

This work is organized as follows. Sections 2 and 3 present the observations and the technique used to fit the CC light curves, respectively. Section 4 shows the color–magnitude diagrams and peak-to-peak amplitudes; in Section 5 we illustrate the PL , PLC , and PW relationships obtained for the SMC CCs and the associated results; a brief final Section 6 summarizes the paper.

2. SMC CLASSICAL CEPHEIDS IN THE VMC SURVEY

As referred to above, the two survey projects that identified CCs in the SMC are OGLE III Soszyński et al. (2010) and EROS 2 (Tisserand et al. 2007). The areas covered by the two surveys overlap almost completely, although OGLE III extends more towards the East, whereas EROS 2 covers a small corner in the North-West where OGLE III data is not available (see Fig. 4 in Moretti et al. 2014, for a comparison).

In more detail, Soszyński et al. (2010) reported the identification, the V , I light curves, and the main characteristics (periods, mean magnitudes, etc.) of 4630 CCs in the SMC. The EROS 2 collaboration provided us with a list of CC candidates that was analyzed as described in Moretti et al. (2014) to reject contaminating binaries, resulting in 151 CC candidates. Among these objects, only about 20 were located outside the area investigated by OGLE III. A quick comparison of the PW in the V , I bands¹⁶ revealed that the EROS 2 CC candidates were severely contaminated by other types of variables (typ-

¹⁵ However the possibility that they are old stars that underwent collisional or binary mergers cannot be excluded (see, e.g. Marconi et al. 2004, and references therein)

¹⁶ The Wesenheit magnitude in this case is defined as $W(V, I) = V - 2.54(V - I)$. Note that EROS 2 observations were carried out using custom B_{EROS2} and R_{EROS2} filters that can be approximately converted to the Johnson V , I bands using the transformation provided by Tisserand et al. (2007).

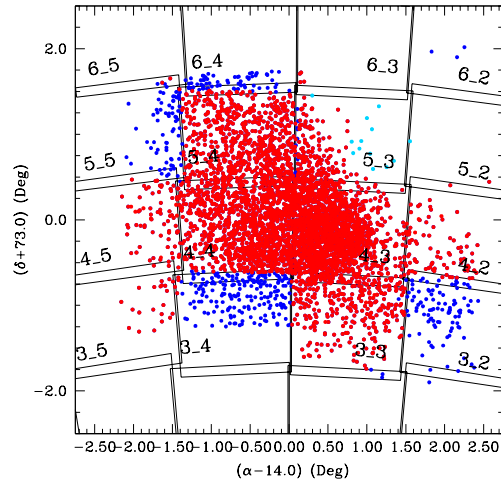


Figure 1. Map of the CCs in the SMC. Red and blue filled circles represent pulsators present in the OGLE III catalog and indicated whether or not they have been observed by the VMC Survey, respectively. Light blue symbols show the 13 Cepheids identified on the basis of the EROS 2 data (Tisserand et al. 2007; Moretti et al. 2014).

ically Type II Cepheids or Anomalous Cepheids) or by other unknown objects. To avoid including spurious objects in our sample, we decided to use only OGLE III data in the area covered by this survey, and to consider only the ~ 20 EROS 2 CC candidates in the (small) area covered by this survey but not by OGLE III. After removing from this small sample those objects that were found to lie very far from the OGLE III PW , we ended up with 13 bona fide CC candidates in the EROS 2-only field.

In this paper we present results for the CCs included in 11 tiles (each tile is 1.5 deg^2 on the sky) completely or nearly completely observed, processed, and catalogued by the VMC survey as of 2015 March 9 (including observations obtained until 2014 September), namely the tiles SMC 3.3, 3.5, 4.2, 4.3, 4.4, 4.5, 5.2, 5.3, 5.4, 6.3, and 6.5. Figure 1 shows the spatial extent of the VMC tiles across the SMC body. The completed tiles do not cover the entire area surveyed by OGLE III. However, given the high concentration of CCs in the central body of the SMC, the number of pulsators included in the completed VMC tiles is about 90% of the total OGLE III sample. Table 1 lists the coordinates of the quoted tiles, as well as the number of CCs included in each tile.

In total, we were able to study 4159 objects of the 4630 OGLE III sample. To this number we have to add the 13 CCs from the EROS 2 data, leaving us with a final sample of 4172 CCs. The classification of the investigated pulsators in terms of Fundamental (F), First Overtone (FO), Second Overtone (SO), and mixed modes (F/FO, FO/SO, F/FO/SO, FO/SO/TO, where TO stands for Third Overtone) is shown in Table 2.

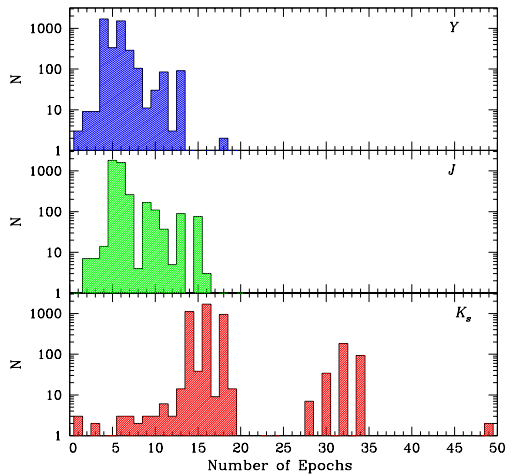


Figure 2. Histogram of the numbers of epochs in each photometric band.

A general description of the observing strategy of the VMC survey can be found in Cioni et al. (2011). The procedures adopted to study the variable stars were discussed in detail by Ripepi et al. (2012a,b); Moretti et al. (2014); Ripepi et al. (2014b, 2015). However, it is worth recalling that the VMC K_s -band time-series observations were scheduled to span 13 separate epochs distributed over several consecutive months. This observing strategy permits one to achieve well-sampled light curves for different types of variable stars, including RR Lyrae variables and Cepheids of all types. As for the Y and J bands, the nominal number of epochs is four (two of these epochs are obtained with half exposure time) and may be acquired during the same night given that monitoring in these filters was not planned. However, a few additional epochs are usually available for each tile (especially in the K_s -band), because some observing blocks (OBs) were executed outside of our specifications (typically for seeing values exceeding 0.8–1.0 arcsec), but the data were still useful since the CCs are relatively bright. In addition, there is a small overlap between the tiles. Consequently, the CCs present in multiple tiles possess at least twice the scheduled number of epochs. Given the high concentration of CCs in the contiguous tiles SMC 4.3, 4.4, 5.3, and 5.4 (see Fig. 1), we have more than 320 CCs whose light curves contain more than ~ 28 phase points. This is also shown in the bottom panel of Fig. 2, where the bimodal distribution of epochs in the K_s band is clear. From the figure, note that there are a few dozen stars with fewer than 13 epochs in K_s . This can happen when the sources are located in underexposed areas and/or are affected by bright neighbours or bad pixels. We were still able to analyze these stars thanks to our template-fitting procedure (see Section 5).

The same considerations hold for the Y and J bands, whose epoch distributions are shown in the top and mid-

dle panels of Fig. 2, respectively. In this case, the number of CCs with more than 10 epochs is 213 and 321 in the Y and J bands, respectively. Similarly, the number of CCs with more than five epochs is 2121 and 2343 in Y and J , respectively.

The VMC data were processed with the pipeline (Irwin et al. 2004) of the VISTA Data Flow System (VDFS, Emerson et al. 2004) and the photometry is in the VISTA photometric system (Vegmag=0). The time-series data analyzed in this work were downloaded from the VISTA Science Archive¹⁷ (VSA, Cross et al. 2012). Details about the data reduction can be found in the aforementioned papers. However, we briefly recall that (i) the pipeline applies a correction to the photometry of stars close to the saturation limit (Irwin 2009). This task is very useful, because long-period CCs are very bright ($K_s \sim 12$ –13) mag. The time-series photometry of these variables takes advantage of the VDFS capability to deal with the images for saturation, although the corrections applied do not always guarantee a full recovery of the data. (ii) The VSA processing produces quality flags for each star that are valuable to understand if the images have problems. This information is important for the following analysis.

To obtain the Y , J , and K_s light curves, the OGLE III (and EROS 2) catalog(s) of CCs described above were cross-correlated against the VMC catalog, taking all counterparts from the OGLE III and EROS 2 positions, regardless of their separation on the sky. About 95% of the objects have positions in agreement with those measured by OGLE III and EROS 2 within less than $0.1''$. Among the remaining 186 stars, 67 have a separation larger than $0.5''$ and are likely misidentifications. We will come back to these objects below.

The typical quality of the light curves obtained is illustrated in Fig. 3 for two F pulsators with very different periods. VMC photometry for the 4172 stars analysed in this work is reported in Table 3. The complete version of the table is available online at the journal site.

3. TEMPLATE-FITTING PROCEDURE

Given the large number of light curves to analyze, it was convenient to find an automatic way to process the data. Our aim is to obtain an analytical or empirical model light curve that fits the observed one. This model can subsequently be used to measure the mean magnitude and the peak-to-peak amplitude for each variable. The usual way to carry out such a task is to use truncated Fourier series, adding as many harmonics as needed to obtain a good fit to the data (Schaltenbrand & Tammann 1971). However, this kind of approach would not be useful in our case, because the presence of significant gaps in the light curve would lead to strong and unrealistic oscillations in the Fourier series.

Hence, we decided to use template light curves to fit the data. Following the pioneering work by Freedman (1988), templates to fit CC light curves based on only a few epochs in the NIR bands have already been presented and used by Soszyński et al. (2005); Inno et al. (2013, 2015). The typical approach in these studies consists of the following steps: (1) adopting templates constructed based on well-sampled CC J, H , and K_s light

¹⁷ <http://horus.roe.ac.uk/vsa/>

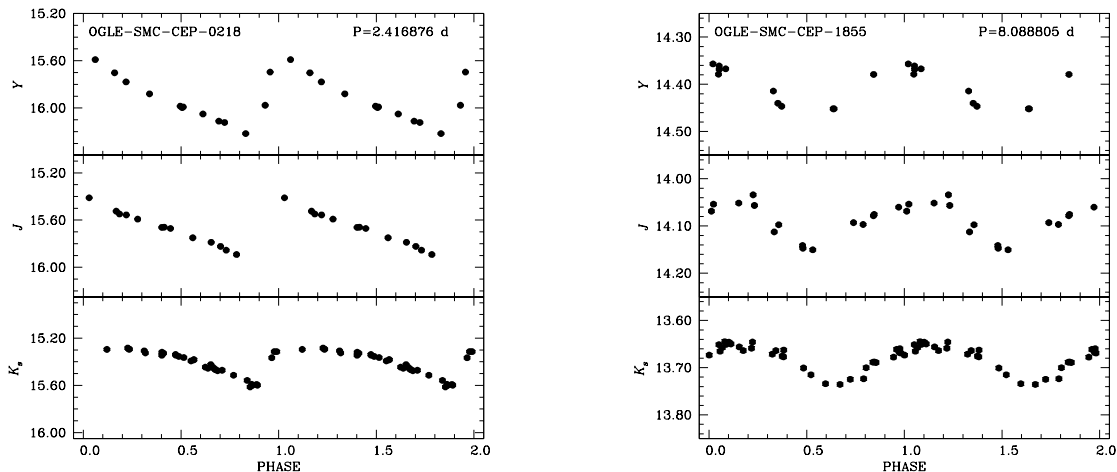


Figure 3. YJK_s light curves for the labelled Cepheids. The errors are of similar size or smaller than the size of the symbols. Note the quality of the data and the change in amplitude and shape of the light curve going from the Y to the K_s bands.

curves (Galactic or MC objects); (2) scaling the template amplitude using fixed amplitude ratios (e.g., $A(J)/A(V)$, with some dependence on period); (3) adopting literature period and epoch of maximum light to phase-match the template and the observed data. This technique is valuable, since it allows one to obtain an estimate of the average magnitude of a CC based on just one or two observed phase points. At the same time, given the uncertainties on the amplitude ratios and on the ephemerides, these estimates can easily be affected by errors as large as 5% (see also Sect. 3.3), despite the quite low amplitudes of the light curves in the NIR bands.

Our approach is fundamentally different from that outlined above (e.g., by Inno et al. 2013). Indeed, the availability of an average of ~ 5.7 , 6.3 , and 16.7 phase points in Y , J , and K_s , respectively, allows us to safely rescale our templates in amplitude and phase match them using our observations directly. This procedure eliminates most of the uncertainties of the “classical” template method, because *we do not have to rely on any fixed amplitude ratio to scale the templates in amplitude, nor do we have to use the literature epoch of maximum as reference to phase match the template and the observed data.*

3.1. Template construction

The first step of our procedure was the construction of the templates. To this end, we visually inspected a large number of light curves, trying to select those with the most often recurring shapes, and at the same time, those exhibiting precise light curves. Particular care was devoted to covering a broad range of periods. This search was rather simple in K_s , since in this band we have dozens of well-sampled and precise light curves for any period. However, we had fewer choices in Y and J , given the much smaller number of well-sampled light curves in those filters.

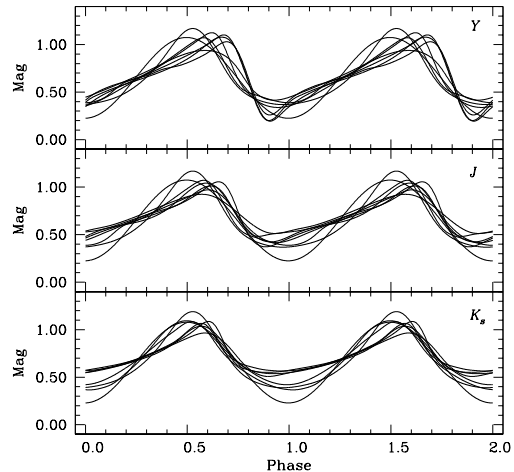


Figure 4. Adopted templates in the YJK_s bands.

At the end of this process, we concluded that a set of eight different templates for each band could reproduce the variety of shapes exhibited by the observed light curves.

Our templates were constructed as truncated Fourier series of the form

$$m(\phi) = a_0 + \sum_{k=1}^N [a_k \cos(2\pi k\phi + \Phi_k)], \quad (1)$$

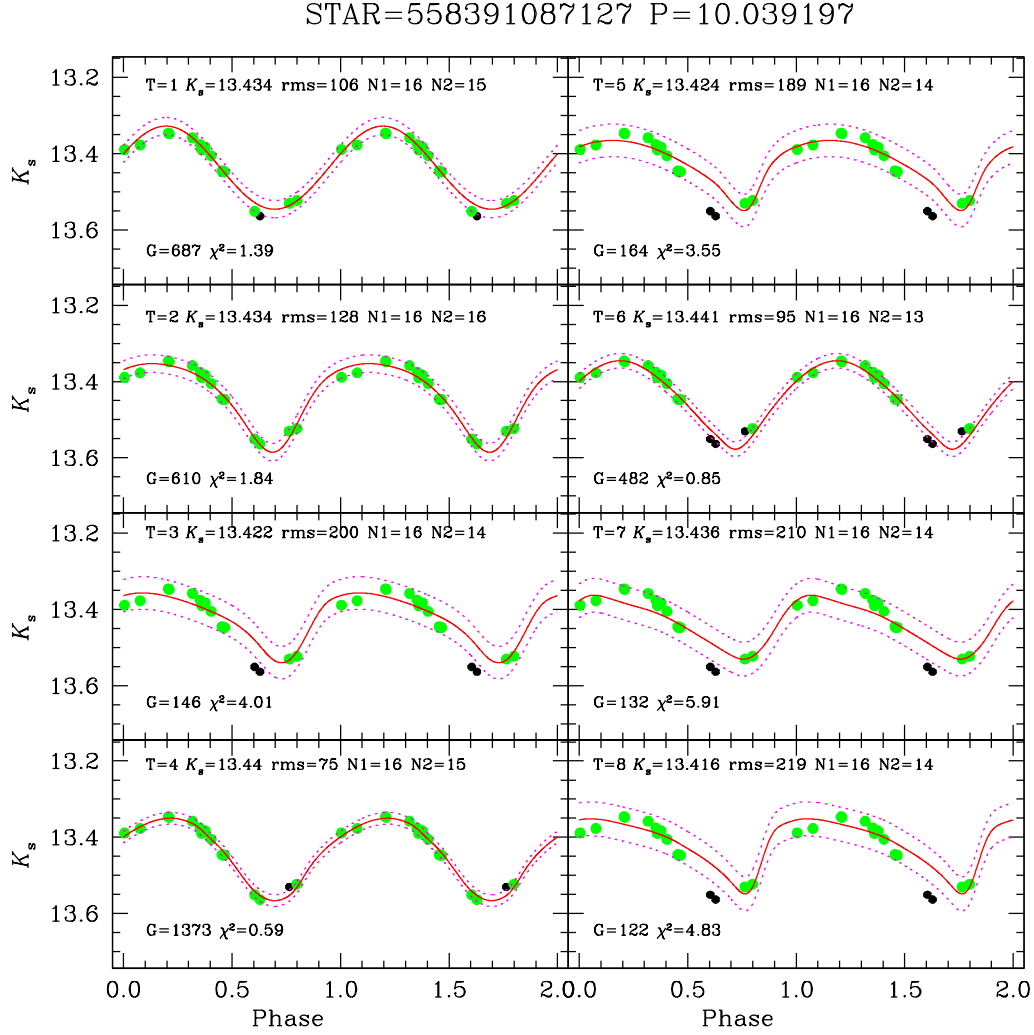


Figure 5. Example of our template-fitting procedure in the K_s band. Each of the eight panels shows the K_s light curve (green and black filled circles show the data points used and rejected in the fitting procedure, respectively). The solid lines are the template curves (labelled with “T” in each panel, with increasing numbers from 1 to 8), properly scaled in amplitude and shifted in phase. The dashed lines represent the $\pm 2\sigma$ template curves: all data points beyond these lines are marked in black and not included in the fitting procedure. The other labels in each panel are: K_s = mean magnitude of the curve needed to fit the data with the template; r.m.s. = root mean square of the fit residuals in mmag; $N1$ = total number of data points in the light curve; $N2$ = number of data points used in the fitting procedure; G = goodness parameter (see the text); $\chi^2 = \chi^2$ of the fit (see the text). In this case, the best template is T4.

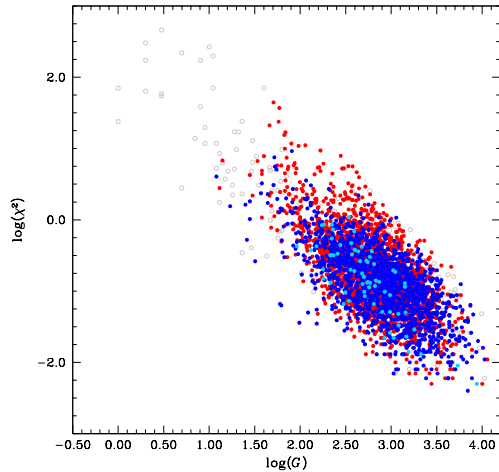


Figure 6. Goodness versus χ^2 in the K_s band for the target CCs. F, FO, and SO pulsators are shown as red, blue, and light blue filled circles, respectively. The gray open circles show the objects excluded from the analysis on the basis of their location near the $PW(K_s, V)$ relation (see Section 5).

where m is the magnitude, ϕ are the phases of the template light curves, a_0 is the zero point, which is zero by definition, N is the number of terms of the series, and a_k and Φ_k are the amplitudes and phases of each term of the series, respectively. The first step consisted of fitting the selected observed light curves with splines in order to have smooth, densely sampled curves to be passed to the Fourier-series fitting program. This was needed to avoid spurious oscillations in the Fourier-series fit due to possible small gaps or undersampling at maximum/minimum of the light curves. This way, we actually constructed six of the eight different templates adopted for each filter. They are listed in Table 4, from T3 to T8. As for the two remaining templates, T1 simply consists of a pure cosine function for all filters (which is why the T1 template is not included in the table), while T2 reproduces a smooth curve which can often be observed in all of the Y , J , and K_s bands for a broad range of periods (see T2 in Table 4). The shapes of the eight templates in all three filters are shown in Fig. 4.

3.2. Template fitting

The template-fitting procedure includes the following steps:

- Scaling the templates with amplitude ratios, e.g., $A(K_s)/A(I)$, where we take $A(I)$ from the OGLE III survey and the coefficients of these ratios from Soszyński et al. (2005). Similarly, the template is phase-matched with the observations using the ephemerides from OGLE III. The purpose of this step is *only* to provide a first-guess average magnitude for the target star and, in turn, to remove the most obvious outliers. In practice, we

simply estimate the template values at the phases of the observed point and calculate the average difference between observed and calculated values, which is the approximate mean magnitude of the star.

- Recalculating the template by varying its initial phase to find the phase shift that minimizes (by means of a least-squares fit) the difference data–template. This step provides an improved average magnitude (of the order of a few hundredths of mag).
- Recalculating the template by varying its amplitude to find the amplitude scaling that minimizes (by means of a least-squares fit) the difference data–template. This step provides a further improvement of the average magnitude (again, a few hundredths of mag).
- Fine-tuning outlier removal (at 2σ and 3σ levels in K_s and in Y, J , respectively; the difference is because in Y, J we have many fewer phase points than in K_s and, hence, we can simply remove obvious outliers) and final average-magnitude calculation (in intensity).

This procedure is applied to each template (in each band). Next, we need a tool to choose the template that optimally represents the data. After several trials and visual inspections of the resulting fits, we devised two main useful diagnostics. The first is the usual χ^2 minimization, defined as

$$\chi^2 = \frac{1}{N} \sum_{\phi=0}^1 \left(\frac{m(\phi)_{\text{obs}} - m(\phi)_{\text{temp}}}{\sigma(m(\phi)_{\text{obs}})} \right)^2, \quad (2)$$

where N is the total number of phase points, m_{obs} and m_{temp} are the magnitudes of the observed and computed light curves, respectively, and $\sigma(m_{\text{obs}})$ is the magnitude uncertainty per phase point.

The second criterion was devised empirically to take into account the fact that the smallest residuals can result from application of the wrong template simply because the outlier-removal process is too aggressive. Thus, we designed a *Goodness* (or G) parameter, defined as

$$G = \text{int} \left[\left(\frac{1}{\sigma} \right)^2 \left(\frac{N_U}{N_T} \right)^4 10^6 \right], \quad (3)$$

where σ is the r.m.s. of the fit and N_U and N_T are the numbers of phase points used in the fit and the total number of phase points, respectively. By definition, the first factor of G tends to favor templates that give the smallest r.m.s. values, while the second factor favors those that remove the lowest number of outliers. The balance of these two features yields, in general, an automatic decision about the best templates that is in agreement with visual inspection of the fitting procedure. The value of G can be used not only to choose the best template, but also as a more general indicator of the quality of the data and of the relative fitting procedure. Indeed, in general high values of G (in our case, typically $G > 100$) mean good data (and good fits), while lower values usually indicate

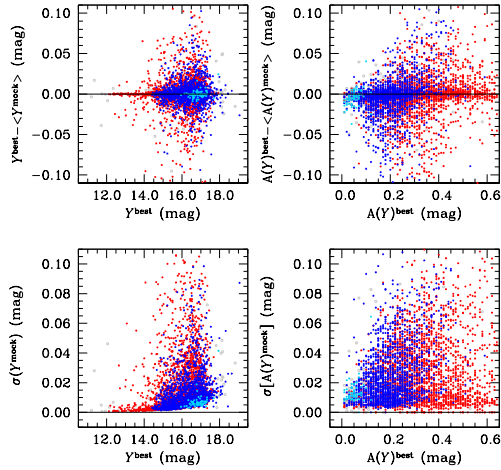


Figure 7. Results from the Monte Carlo experiments in the Y band. The top left-hand panel shows, for each star, the difference between the magnitude obtained with the best-fitting template (Y^{best}) applied to the real data and that resulting from averaging over the 100 Monte Carlo experiments ($\langle Y^{\text{mock}} \rangle$). The bottom left-hand panel shows the r.m.s. of Y^{mock} as a function of Y^{best} . The top and bottom right-hand panels are similar to those on the left but display the peak-to-peak amplitudes instead of the magnitudes (in the Y band). The color coding is the same as in Fig. 6.

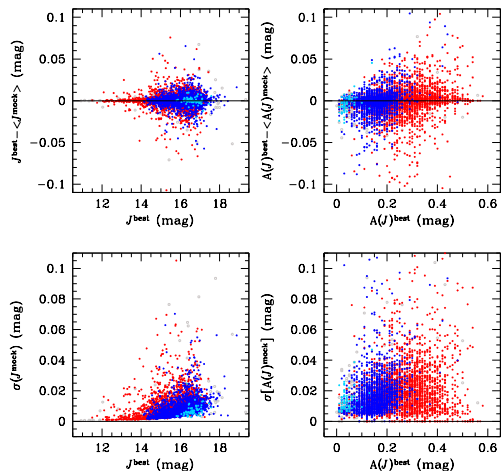


Figure 8. As Fig. 7 but for the J band.

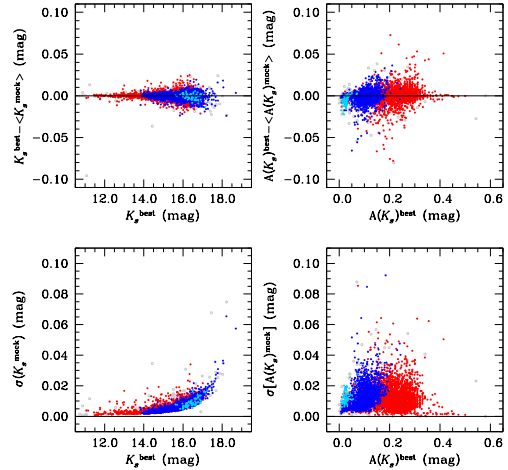


Figure 9. As Fig. 7 but for the K_s band.

significant scatter in the light curves. Extremely high values of G (i.e., $G > 10,000$) are also rather suspect because non-variable stars, exhibiting completely flat light curves (which happens, for example, when non-variable stars are considered owing to a coordinate mismatch with OGLE III Cepheid data) are expected to yield extremely high values of G . Not surprisingly, the G parameter is anti-correlated with the corresponding χ^2 value: the higher G is, the lower the χ^2 becomes. An example of our template-fitting procedure can be found in Fig. 5 (note that in this case the best template is T4), while the anti-correlation between G and χ^2 is shown in Fig. 6.

3.3. Monte Carlo simulations

As an additional check of the reliability of the template-fitting procedure, and to estimate in a more quantitative way the precision achieved, we decided to use extensive Monte Carlo simulations. In practice, for each star (and for each filter), 100 different mock time series were created on the basis of the observed data, to which Gaussian noise was added with σ 's corresponding to the average uncertainty on the phase points for the star of interest (different σ 's were calculated for different filters). The template-fitting procedure outlined above was hence repeated 100 times and the average magnitude and r.m.s. were calculated. We then compared these quantities with those calculated from the observed data. The results of this exercise are summarized in Figs 7, 8, and 9. The top left-hand panels in each figure show the difference between the magnitude obtained with the best-fitting template (Y^{best} , J^{best} , K_s^{best}) applied to the actual data and that resulting from averaging over the 100 mock light curves ($\langle Y^{\text{mock}} \rangle$, $\langle J^{\text{mock}} \rangle$, $\langle K_s^{\text{mock}} \rangle$). Similarly, the bottom left-hand panels show the r.m.s. of Y^{mock} , J^{mock} , K_s^{mock} as a function of Y^{best} , J^{best} , K_s^{best} . These figures testify to the high precision reached in the

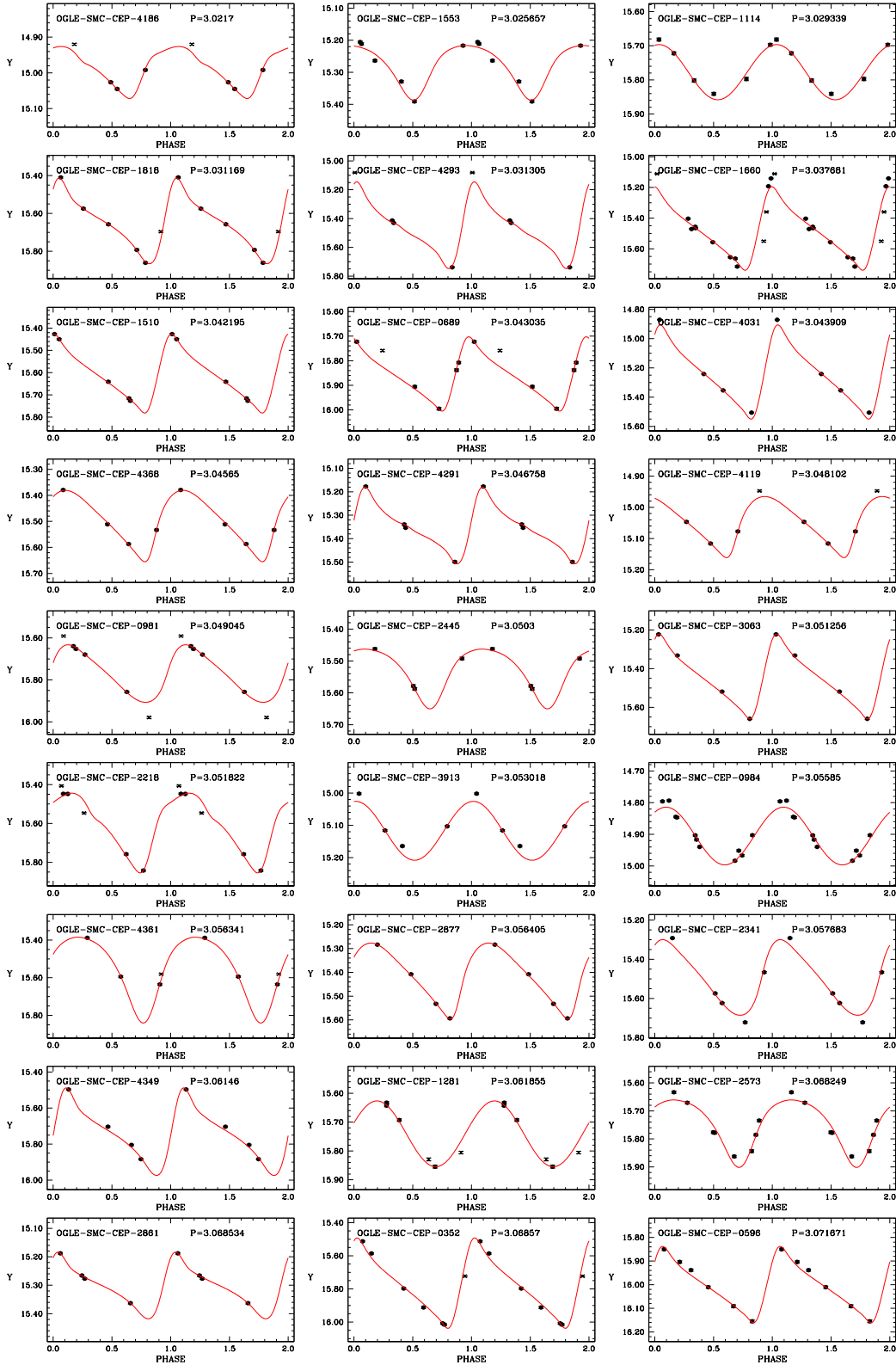


Figure 10. Light curves in the Y band with superimposed the best template fit for a sample of 27 CCs analyzed in this paper. Filled circles and crosses show the data points adopted and discarded during the fitting procedure, respectively. The solid red line represents the template fitted to the data. The OGLE III or EROS 2 identification and the period of the variable are also reported. The complete figure, including the light curves for the full data set of 4172 CCs, is published in its entirety in the electronic edition of the *Astrophysical Journal*. A portion is shown here for guidance regarding its form and content. Note that in the electronic version of the figure, the CC light curves are shown in order of increasing period (see caption of Table 5 for details).

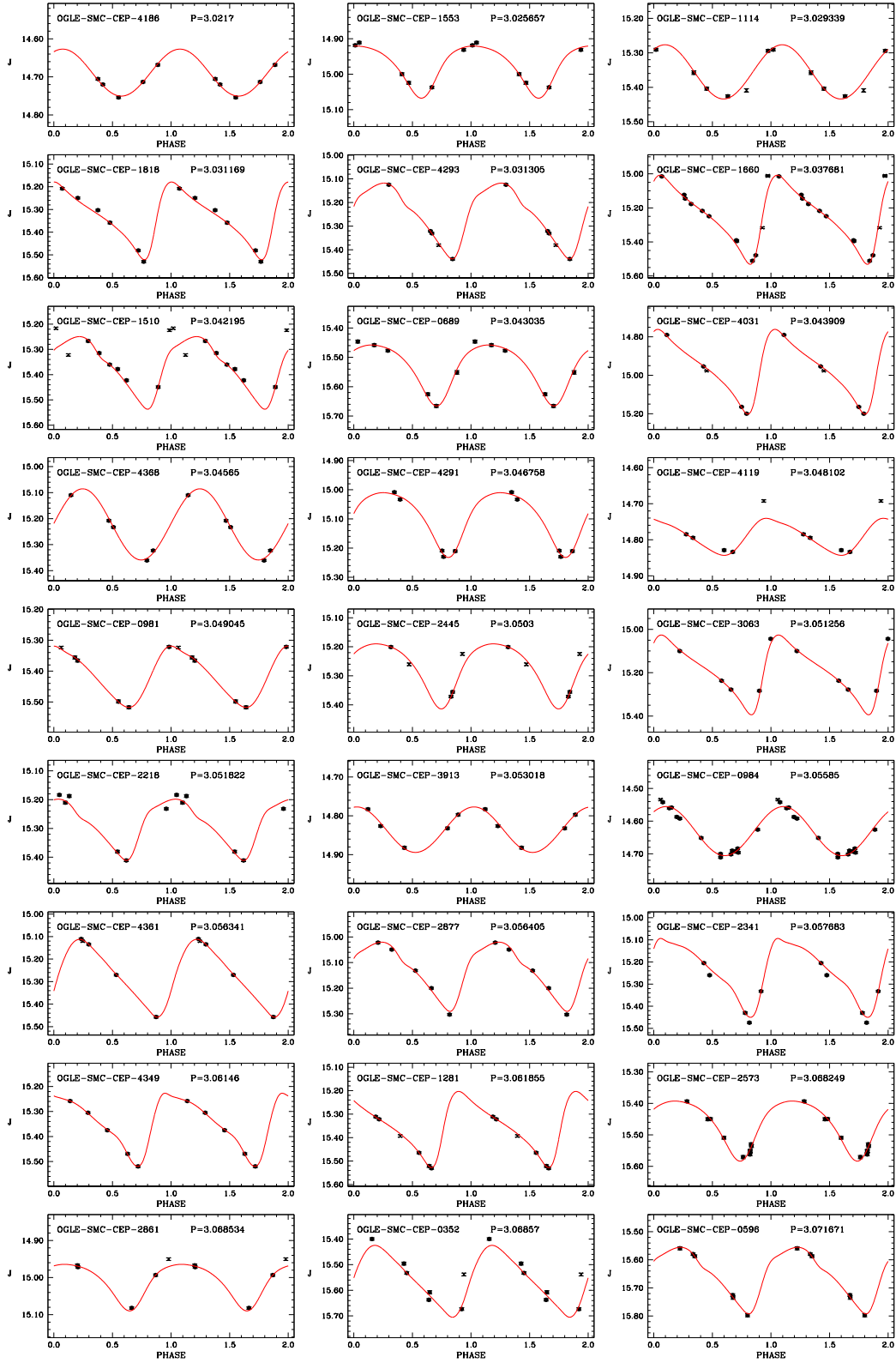


Figure 11. As Fig 10 but for the J band.

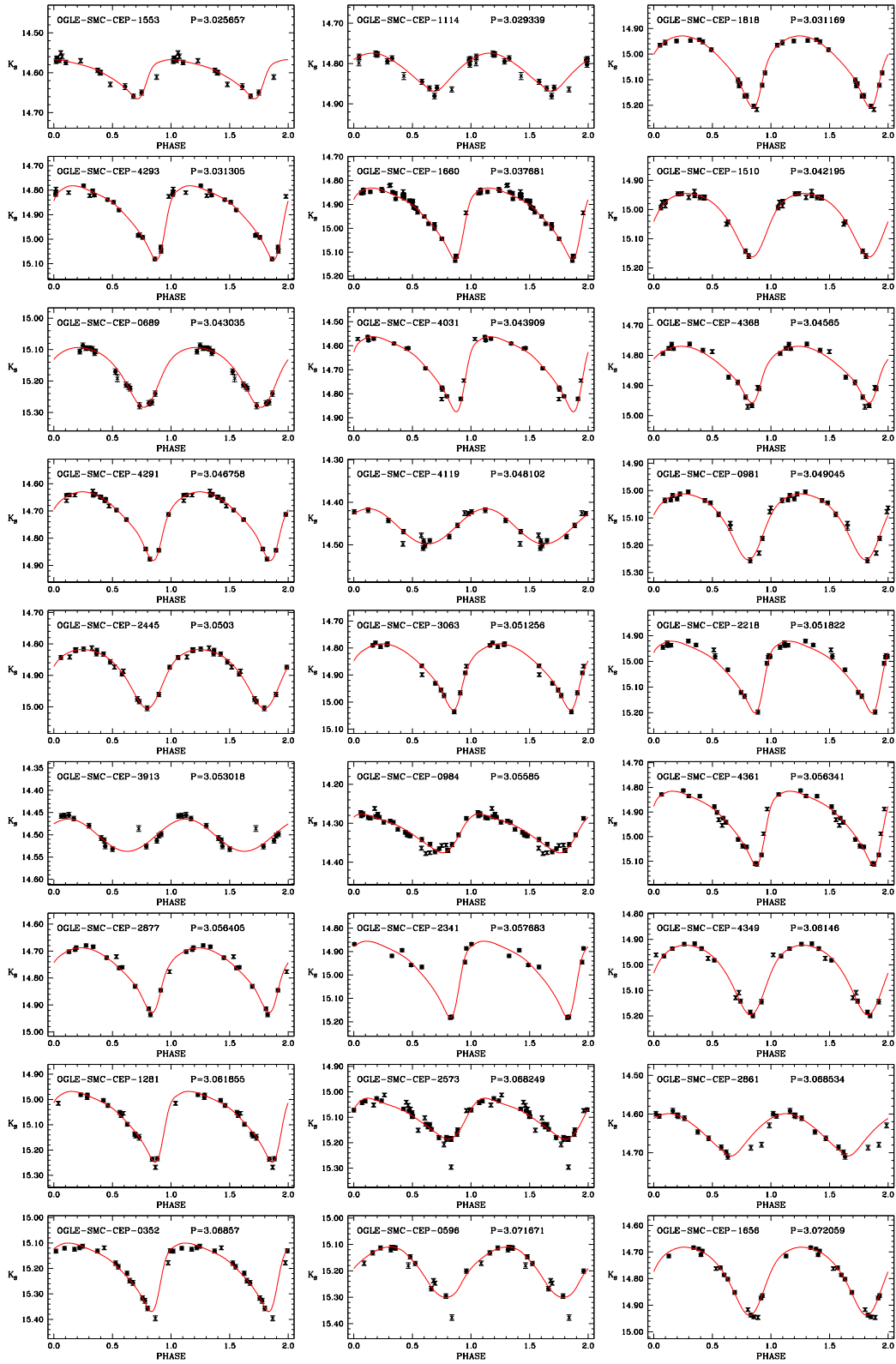


Figure 12. As Fig 10 but for the K_s band.

K_s band, where 84% and 99% of the stars have errors on the intensity-averaged magnitudes of ≤ 0.01 mag and ≤ 0.02 mag respectively. Only 1% and 0.1% of the CCs analyzed here have uncertainties > 0.02 mag and > 0.05 mag, respectively. The results are less favorable in the J band and even worse in Y . In fact, in these bands the corresponding percentages drop to (68%, 93%, 7%, and 0.8%) and (56%, 78%, 22%, and 5.5%) in the J and Y bands, respectively. The worse results in Y are mainly due to the fact that (a) the peak-to-peak amplitude in this filter is significantly larger than that in the J band (consequently, it is more difficult to estimate the average magnitudes from undersampled light curves) and (b) we have, on average, fewer phase points in Y than in J (~ 5.6 versus ~ 6.3).

The top and bottom right-hand panels in Figs 7, 8, and 9 display essentially the same results as the panels on the left, but for the peak-to-peak amplitudes instead of the intensity-averaged magnitudes. Again, the results for the amplitudes in the K_s band are very good, while the uncertainties become significantly larger for the J and, especially, the Y filters.

On the basis of the Monte Carlo experiments, we decided to assign as uncertainties to the intensity-averaged magnitudes and peak-to-peak amplitudes the values shown in the bottom panels of Figs 7, 8, and 9.

The light curves and the best-fitting templates found with the procedure outlined in this section are reported in Figs 10, 11, and 12 for the Y , J , and K_s bands, respectively. These figures display the data for a subsample of 27 CCs; figures including the full data set of 4172 objects are available in the electronic version of this paper on the journal's website.

Similarly, Table 5 reports the main physical quantities derived on the basis of the fitting procedure, namely the intensity-averaged magnitude for each variable (and each filter), the peak-to-peak amplitudes, and the relative errors calculated by means of the Monte Carlo experiments.

Finally, we recall that the Y , J , and K_s photometry described in this work is defined in the VISTA system. It is possible to compare our data with measurements in the widely used 2MASS system (Two Micron All Sky Survey Skrutskie et al. 2006) after applying the system transformations made available by the Cambridge Astronomy Survey Unit (CASU)¹⁸: $(J-K_s)^{2M}=1.081(J-K_s)^V$, $J^{2M}=J^V+0.07(J-K_s)^V$, and $K_s^{2M}=K_s^V-0.011(J-K_s)^V$. No transformation is provided in Y since 2MASS did not observe in this filter. However, it is possible to “standardize” the Y band by applying a color equation that, at present, is available only as a function of the $(J-H)$ color (and is therefore of no use to us). A new transformation using the $(J-K_s)$ bands is being derived by CASU and will be available within a few months.

Since the intrinsic $\langle J \rangle - \langle K_s \rangle$ colors of the CCs investigated here typically range from 0.1 mag to 0.6 mag, the VISTA and 2MASS K_s can be considered equivalent for CCs (see Fig. 13) to a very good approximation (better than ~ 5 mmag), although the corrections needed in the J band can be significant.

4. AVERAGE MAGNITUDES, COLORS AND PEAK-TO-PEAK AMPLITUDES

We constructed color-magnitude diagrams for the entire sample of CC analyzed here, distinguishing them by the different types of pulsation. The results are shown in Fig. 13. The middle and right-hand panels of this figure display the comparison in the $K_{s,0}, (J-K_s)_0$ and $K_{s,0}, (V-K_s)_0$ planes of the observed data with the theoretical instability strips for F, FO, and SO CCs. The models, calculated for $Z = 0.004$ and $Y = 0.25$, have been taken from Bono et al. (2000, 2001a,b). We note that the models are in the JHK Johnson system. Thus, we have to converted them into the VISTA system, adopting the VISTA-2MASS relations referred to in the previous section, as well as the color transformations available from Bessell & Brett (1988) and Carpenter (2001). As a result, we obtained the following approximate equations:

$$K_s^V = K_s^J + 0.007(V-K)^J + 0.03(J-K)^J - 0.038 \quad (4)$$

$$(V-K_s)^V = 0.993(V-K)^J - 0.03(J-K)^J + 0.038 \quad (5)$$

$$(J-K_s)^V = 0.87(J-K)^J - 0.01 \quad (6)$$

where the superscripts “V” and “J” refer to quantities in the VISTA and Johnson systems, respectively. There is general good agreement between predicted colors and observations, especially for FO pulsators, while for F pulsators the observed instability strip appears to be larger at low luminosities (i.e., short periods) compared with the predictions.

Additional information can be obtained from the color-color diagrams shown in Fig. 14, where the left- and right-hand panels show the $(J-K_s, Y-K_s)$ and $(V-K_s, J-K_s)$ planes, respectively. In both cases, arrows represent the reddening vectors, which are almost parallel to the data distribution, making it almost impossible to use these planes to estimate individual reddening values. It is interesting to note the distribution of the rejected stars (empty gray circles), which is markedly elongated towards red colors (especially in the $(J-K_s, Y-K_s)$ plane). This suggests significant contamination in the K_s band by very red objects, likely red clump or red/asymptotic giant-branch stars, or bright (early-type) background galaxies. The right-hand panel of Fig. 14 shows the theoretical instability strip, now visible as an almost straight line passing, as expected, through the middle of the data distribution. Indeed, at fixed effective temperature, the position in the color-color plane is unequivocally determined by the adopted effective temperature-color transformation. Note that the modest broadening of the data (~ 0.07 -0.1 mag) is due to different contributions, namely the photometric errors, blending effects, and/or small metallicity differences, but not to reddening effects (see the direction of the reddening vectors in both planes of Fig. 14).

Figure 15 shows the period versus peak-to-peak amplitude in the K_s band for the target CCs. As far as we know, this is the first time that such a plane has been exploited with such a statistically significant number of objects in an infrared band. An inspection of the figure reveals the clean separation in amplitude of the three dif-

¹⁸ <http://casu.ast.cam.ac.uk/surveys-projects/vista/technical/photometric-properties>

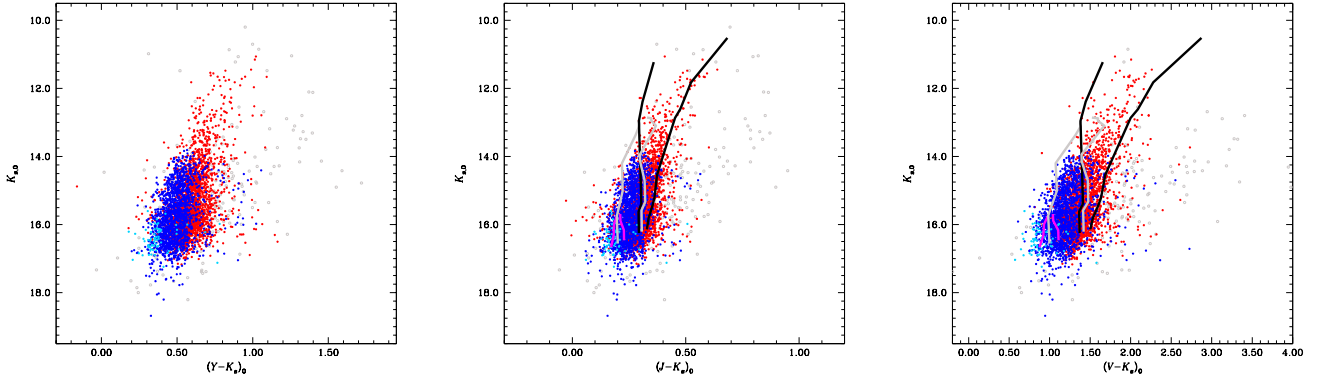


Figure 13. The left, middle, and right panels show the color–magnitude diagrams for the $(K_s, Y - K_s)$, $(K_s, J - K_s)$, and $(K_s, V - K_s)$ combinations of magnitudes and colors, respectively. The color coding is the same as that in Fig. 6. The middle and right-hand panels also show the theoretical instability strips for F (black lines), FO (gray lines), and SO (magenta lines) CCs, respectively. The models, calculated for $Z = 0.004$ and $Y = 0.25$, have been taken from Bono et al. (2000, 2001a,b).

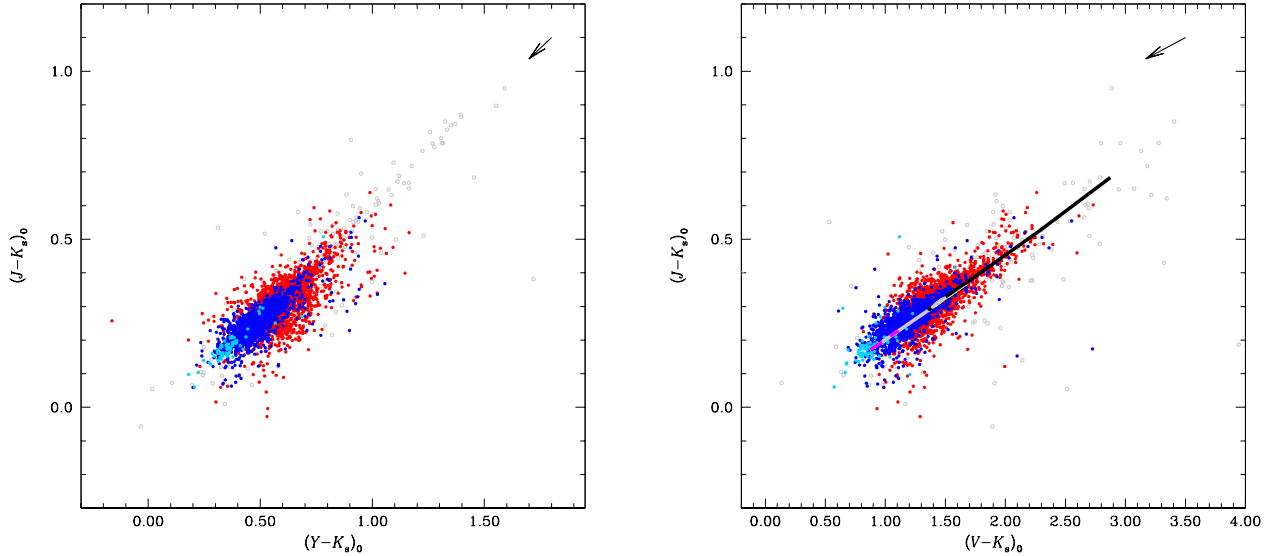


Figure 14. The left- and right-hand panels show the color–color diagrams in the $(J - K_s, Y - K_s)$ and $(V - K_s, J - K_s)$ planes, respectively. The color coding is the same as that in Fig. 6. The right-hand panel also shows the theoretical instability strips from Fig. 13. In both panels, arrows indicate the reddening vectors, calculated for a reddening value $E(V - I) = 0.15$ mag, i.e., approximately three times the average reddening in the SMC, according to the adopted reddening maps of Haschke, Grebel & Duffau (2011).

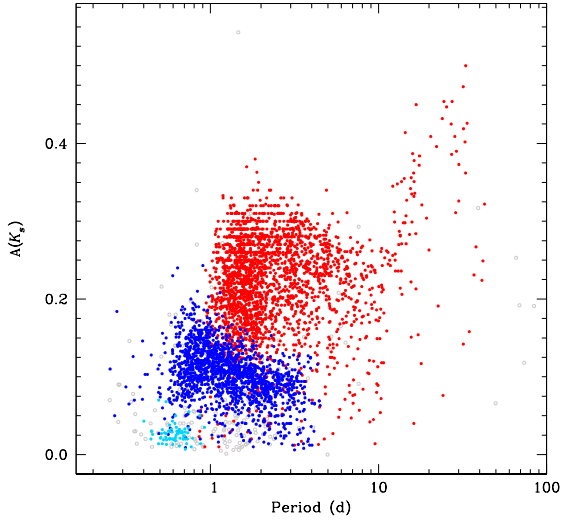


Figure 15. Period versus amplitude in the K_s band for the target CCs. The color coding is the same as that in Fig. 6.

ferent modes. It is interesting to note that the peculiar shape of the distribution of F pulsators, with an increase at about $P = 10$ d and a maximum around $P = 22$ – 24 d, resembles a similar trend observed in the visual V band for the Galactic CCs (Bono et al. 2000) and is consistent with theoretical predictions (see their Fig. 6).

We also looked at the peak-to-peak amplitude ratios for different pulsation modes between the K_s and I bands. These values may be useful for authors who want to use the canonical template-fitting procedure. Figure 16 shows the $R(K_s, I) = A(K_s)/A(I)$ ratio versus period for the CCs investigated here. We calculated the ratio between these bands, because our amplitudes are more accurate in K_s relative to Y and J (see Section 5) and OGLE III provides the peak-to-peak amplitudes for all Cepheids investigated here only in the I filter.

Given the rather large scatter in the data (possibly in part due to the presence of binary companions), we decided to average the CCs in period bins, obtaining the light blue and yellow filled circles for F and FO pulsators, respectively (we did not consider the SO CCs because of their very small amplitudes). An analysis of the averaged data reveals the different behavior of F and FO pulsators. $R(K_s, I)$ is almost constant for FO pulsators over the full period range, while for F pulsators it is flat only until $P \sim 2.95$ d. For longer periods there is a steep linear increase of $R(K_s, I)$ with period. Quantitatively, we derived the following equations for F and FO pulsators:

$$\begin{aligned} R(K_S, I)_F &= (0.04 \pm 0.01) \log P + (0.40 \pm 0.01) \\ &\quad (P < 2.95 \text{ d}) \\ R(K_S, I)_F &= (0.26 \pm 0.02) \log P + (0.31 \pm 0.02) \end{aligned} \quad (7)$$

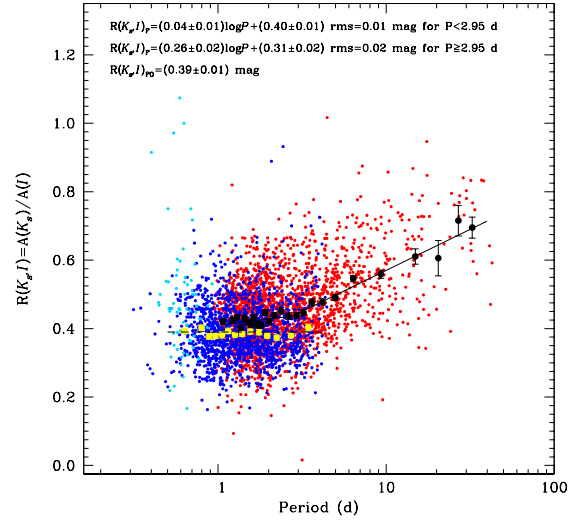


Figure 16. Peak-to-peak amplitude ratios $A(K_s)/A(I)$ for the F, FO, and SO mode pulsators studied here. The I -band amplitudes band are from the OGLE III survey. The color coding of the small filled circles is as that in Fig. 6. The black and yellow filled circles represent the averages in period bins for F and FO pulsators, respectively. The derived analytical ratios are labelled in the figure.

$$(P \geq 2.95 \text{ d}) \quad (8)$$

$$R(K_S, I)_{FO} = (0.39 \pm 0.01). \quad (9)$$

It is interesting to note that the steep change in slope for F pulsators occurs at about the same period where we find a break in the PL , PW , and PLC relations (see next section).

A comparison of our results with those in the literature reveals some differences. Indeed, concerning F pulsators only, Soszyński et al. (2005) suggest using constant values of $R(K_S, I) = 0.49$ or 0.62 for periods $</\geq \sim 20$ d, respectively. Using Eq. 8, for $P \sim 20$ d we obtain $R(K_S, I) = 0.65$, which is fully compatible with Soszyński et al. (2005)'s values. However, it is easy to verify that the agreement is worse for different periods. For example, at $P = 40$ d, we obtain $R(K_S, I) = 0.73$, while at $P = 2$ d $R(K_S, I) = 0.41$. Taking into account that the Soszyński et al. (2005) results have been derived using Galactic and LMC CCs, it is reasonable to hypothesize that part of the discrepancy between our and their findings can be owing to the different metallicities of the adopted CC samples.

We cannot perform a direct comparison with Inno et al. (2015)'s results, because they only provide the ratio of NIR bands with respect to the V band. However, we can compare the trends versus the periods, since they have different data sets for Galactic+LMC and SMC CCs. As a result, Inno et al. (2015) found a break in $R(K_S, I)$ at a period similar to that of Soszyński et al. (2005). This is in contrast with our results (perhaps this is due

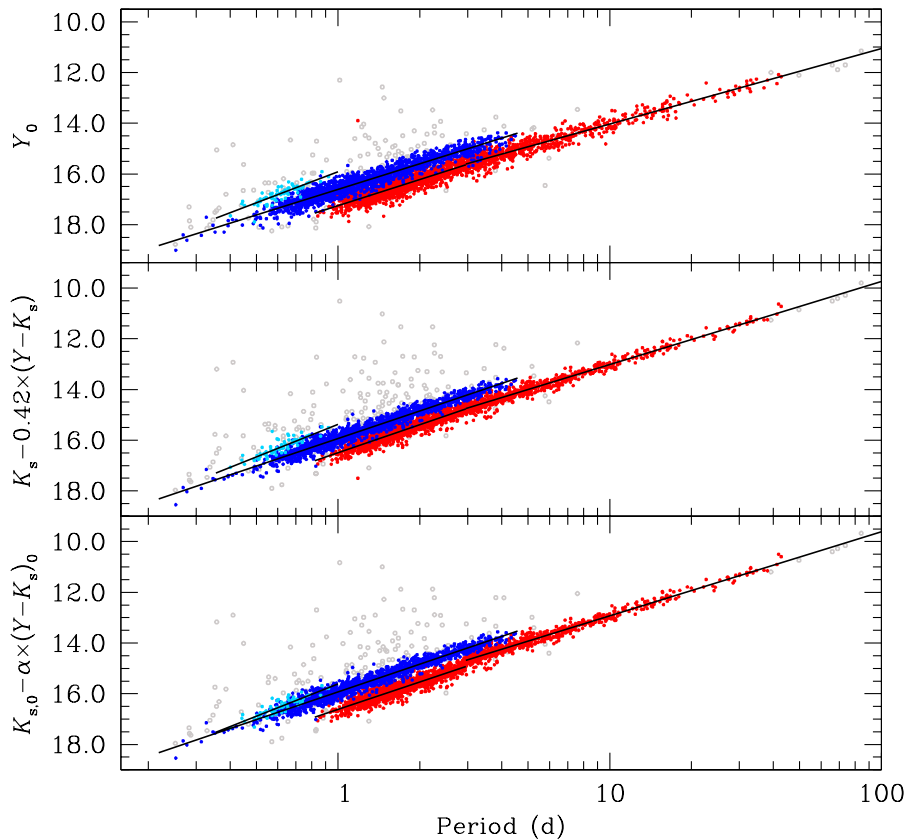


Figure 17. From top to bottom, $PL(Y)$, $PW(K_s, Y)$, and $PLC(K_s, Y)$ relations for the SMC CCs investigated in this paper. The color code is the same as that in Fig. 6. The solid lines represent least-squares fits to the data shown in Table 6. Note that the discontinuity in the bottom panel, both in data and fit, for F-mode pulsators is only due to the visualization procedure (projection from 3 to 2 dimensions).

to the smaller size of their sample). On the other hand, they found systematically lower $R(K_S, I)$ values for SMC CCs, with respect to the Galactic+LMC variables, in full agreement with our results.

5. PL , PLC , AND PW RELATIONS

The data reported in Table 5 allow us to derive several useful relationships, adopting various combinations of magnitudes and colors. In particular, we derived PL relations in Y , J , and K_s , as well as PW and PLC relations for the following combinations: $(K_s, Y - K_s)$, $(K_s, J - K_s)$, and $(K_s, V - K_s)$.

Before deriving the latter relationships we have to take account of the reddening. We adopted the extinction maps of Haschke, Grebel & Duffau (2011), as we already

successfully did in our previous papers (see, e.g., the discussion in Sect. 3 of Ripepi et al. 2015). The reddening values were converted using the following equations: $E(Y - K_s) = 1.80E(V - I)$; $E(V - K_s) = 2.24E(V - I)$; $E(J - K_s) = 0.43E(V - I)$ (Cardelli et al. 1989; Kerber et al. 2009; Gao et al. 2013).¹⁹ The coefficients of the PW relations were calculated in a similar fashion.

To derive the relevant relationships for F, FO, and SO variables, we adopted equations of the form $M1_0 = \alpha + \beta \log P$, $W(M1, M2) = \alpha + \beta \log P$, and $M1_0 = \alpha + \beta \log P + \gamma(M2 - M1)_0$ for the PL , PW , and PLC relations, respectively. Here, $M1$ and $M2$ represent two

¹⁹ The coefficients used in this paper are consistent with the 2MASS system, to which the VISTA system is related.

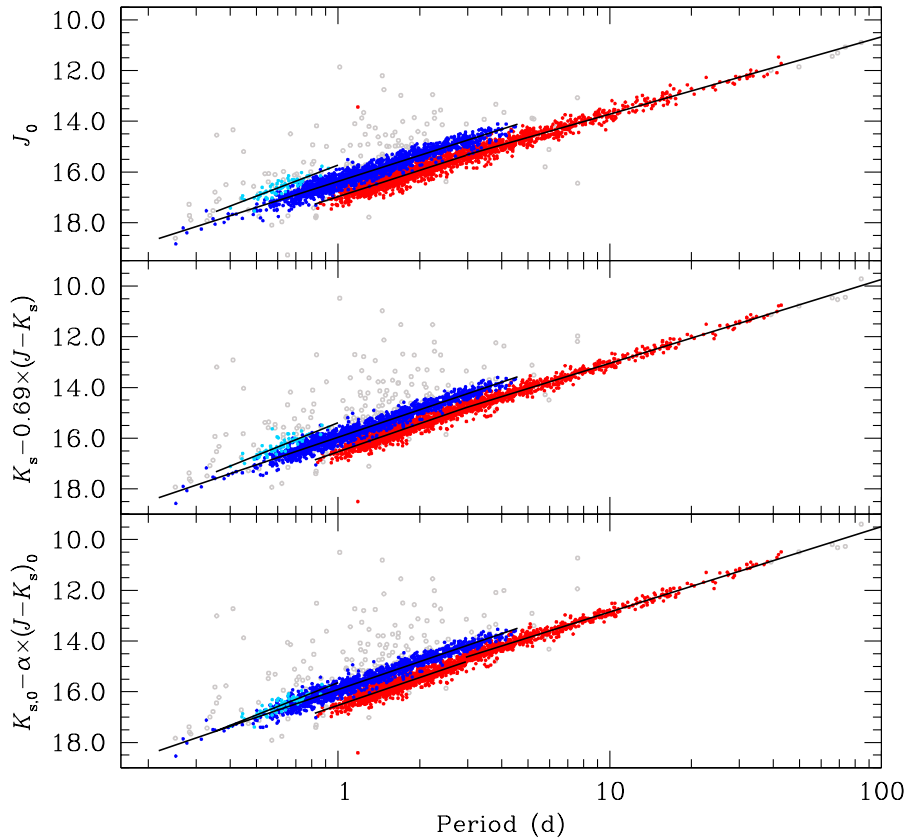


Figure 18. As Fig. 17 but for $PL(J)$, $PW(K_s, J)$, and $PLC(K_s, J)$.

different magnitudes from among V , Y , J , and K_s . The details about the combinations of magnitudes and colors adopted in this paper can be found in Table 6. In order to use the full sample of pulsators, including the double- or multi-mode CCs, we decided to use them with the period of the dominant mode (e.g., F-mode if the star is an F/FO double-mode pulsator, and so on). This procedure is safe, since from our previous investigation of LMC pulsators (Ripepi et al. 2012a) we know that these objects do not exhibit systematic luminosity differences with respect to single-mode objects.

The next step involved checking for the presence of changes in the slope of the different relationships, as found in previous studies in the literature (see, e.g. Subramanian & Subramanian 2015, and references therein). To this aim, we used the PW in V, K_s which was known

from our previous investigation of the LMC CCs, to show a small intrinsic dispersion (see, e.g. Ripepi et al. 2012a), and which is thus particularly appropriate for our purpose. As a result, we found that there is a clear change in slope at $\log P = 0.47$ (~ 2.95 d) for F-mode pulsators, while there is no significant change in slope for FO variables. This was confirmed by the analysis of the PL and PW in different filters and is in agreement with the results obtained in the optical (V, I bands) for the OGLE III sample of F-mode pulsators by Subramanian & Subramanian (2015) (see also references in this paper). However, we do not find the break at $\log P = 0.029$ (~ 1.07 d) that they noticed for FO-mode pulsators. A possible explanation for the break detected at $P \sim 3$ d is that for shorter periods the blue loop of the Cepheid evolutionary track is too short and enters only the reddest

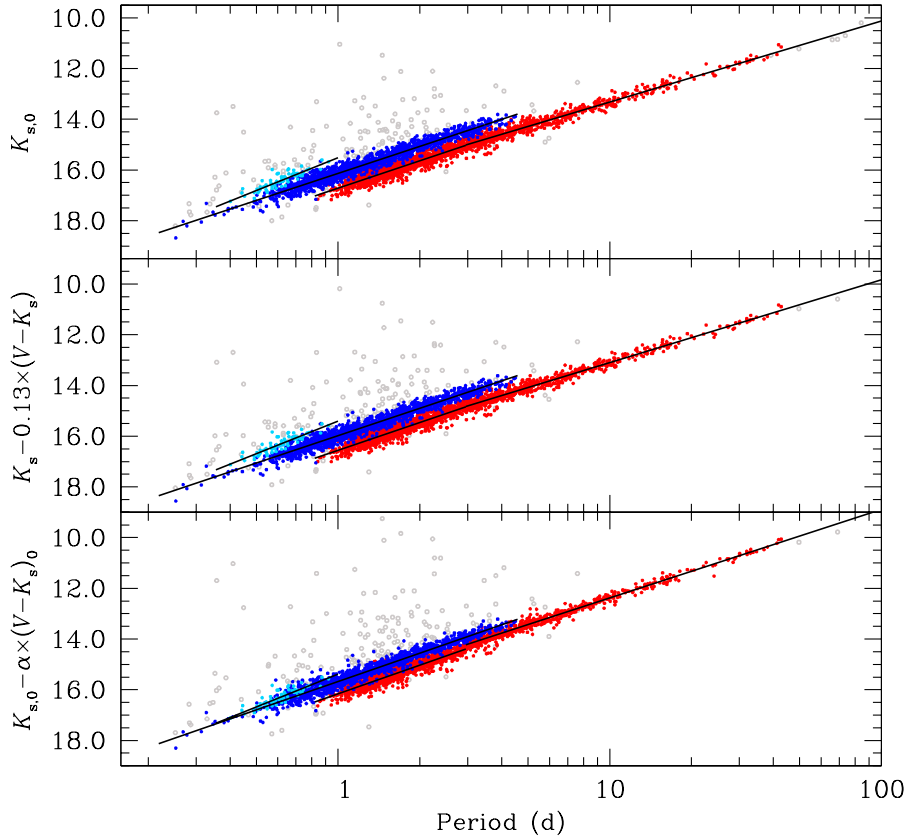


Figure 19. As Fig. 17 but for $PL(K_s)$, $PW(K_s, V)$, and $PLC(K_s, V)$.

part of the instability strip (M. Marconi et al., in prep).

The $PW(V, K_s)$ was also used to analyze problematic objects, identified as clear outliers from these relations. In total, we discarded 223 CCs. We identified different (but often concurrent) reasons for the erratic behavior of these objects (see the final column in Table 5 for details): (i) misidentification: all objects with separation VMC–OGLE III $> 0.2''$ were visually inspected and rejected if they were found to be overluminous in the $PW(V, K_s)$ relation (more than 100 objects were rejected as such); (ii) scattered or heavily undersampled light curves (always low G /high χ^2 values; more than 50 such objects were present); (iii) notes from either OGLE III or VMC, i.e., the presence of flags reporting problems with the images (more than 20 rejections); (iv) saturation (seven objects). Note also that 17 objects with good VMC photometry

were rejected because they lacked OGLE III V -band photometry. Not all outliers can be explained by invoking these reasons; in fact, there are 35 outliers for which we could find no apparent flaws. However, most are faint and all are overluminous. Hence, it is likely that they suffer from blending with bright neighbor stars. The discarded stars are reported separately, both in Table 5 and Figs 10, 11, and 12. Finally, we note that a few other objects were excluded from the derivation of the PL , PW , and PLC relations involving the Y or J bands because of specific problems in these bands. To avoid confusion, these objects have not been highlighted in the table and figures.

On this basis, we performed a least-squares fit to the data to derive all relations, adopting a break at $\log P = 0.47$ ($P \sim 2.95$ d) for F-mode CCs, while all FO- and SO-

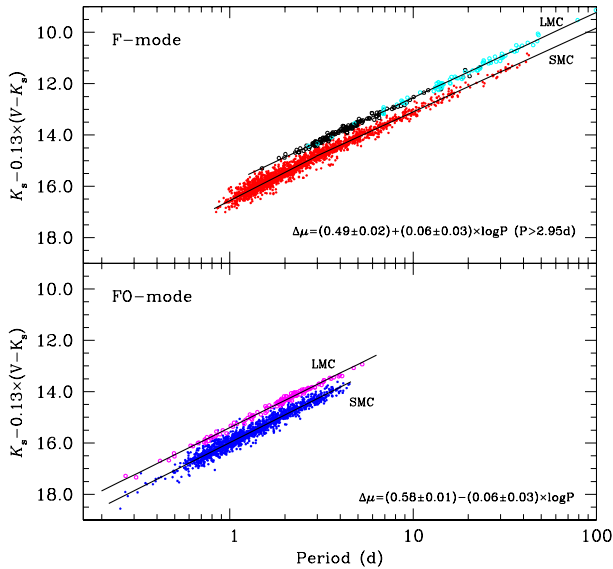


Figure 20. Top: $PW(K_s, V)$ for the LMC and SMC F-mode CCs according to Ripepi et al. (2012a) (black circles), Persson et al. (2004) (light blue circles), and this paper (filled red circles), respectively. Bottom: as the top panel but for FO-mode pulsators in the LMC (magenta circles, Ripepi et al. 2012a) and in the SMC (filled blue circles, this work). In both panels the solid lines represent the best fits to the data (see text for details).

mode pulsators were used together. The results of this work are shown in Table 6 and Figs 17, 18, and 19, where from top to bottom we display the F-, FO-, and SO-mode PL , PW , and PLC relations, respectively. Note that the PLC relations show a distinct discontinuity at $\log P = 0.47$ owing to the way the data are projected in two dimensions. As far as we know, these are the first CC PL , PW , and PLC relations ever derived that involve the Y band. The same is true for SO pulsators, even if in this case the small number of objects available for the calculations (about 70) and their intrinsic faintness did not allow us to obtain PL , PW , and PLC relations to similar precision as those for F and FO pulsators (see Table 6).

The regressions listed in Table 6 (and in Figs 17, 18, and 19) show that the PL relations have, as expected, a larger dispersion with respect to the PW and PLC relations, which show a similar scatter for all combinations of magnitudes and colors, even though the use of $(V - K_s)$ and $(J - K_s)$ give slightly better results. This is not surprising, since the general quality of the Y -band data is (moderately) worse than that in J . In any case, the constancy of the dispersion of all these relations is a clear indication that the elongated structure of the SMC is dominating the intrinsic dispersion of these relations, which we know from LMC studies to be much smaller

(see, e.g. Ripepi et al. 2012a; Inno et al. 2013; Macri et al. 2015).

We can now compare our results with the previous investigation by Inno et al. (2013). These authors derived PW relations for a variety of combinations of magnitudes and colors for SMC and LMC CCs, including the NIR bands J, H, K_s . Their photometric database relies mainly on single-epoch light curves, from which they derived average magnitudes by adopting some literature template light curves and relying on published ephemerides and amplitude ratios (e.g., $A(J)/A(I)$). It is important to note our very different approach with respect to theirs. Indeed, the larger number of observed epochs (especially in the K_s band) allowed us to adopt a template procedure without having to rely on any external information (apart from the periods, see details in Section 5) and which is capable of achieving much higher precision of the intensity-averaged photometry for each individual CC. The relations we can compare with Inno et al. (2013) are the $PW(J, K_s)$ and $PW(V, K_s)$ for F and FO pulsators. The latter authors calculated these relations in different ways, either without taking into account any break or by arbitrarily imposing breaks at $\log P = 0.35, 0.40, 0.45$. Therefore, we can compare the $PW(J, K_s)$ and $PW(V, K_s)$ relations with no break for FO pulsators (Table 1 of Inno et al. 2013) and the $PW(J, K_s)$ relation for F pulsators with a break at $\log P \geq 0.45$ (see Table 3 of Inno et al. 2013)²⁰. To take into account that our photometry is in the VISTA system, while Inno et al. (2013)'s were in the 2MASS system, we have applied the equations discussed in Section 5 to convert Inno et al. (2013)'s relations to the VISTA system. We can now finally perform the comparison with the values listed in our Table 6. We obtain very good agreement for the three PW relations quoted above, in all cases within $\sim 1\sigma$. However, we emphasize that the precision for the individual CC W magnitudes is better in our case given the larger number of observations. This is an important factor when dealing with the structure of the SMC, whose study requires precise individual relative distances.

5.1. The relative distance between SMC and LMC and the absolute distance of the SMC

The relationships derived in the previous Section will be used in a forthcoming paper to study in detail the 3D structure of the SMC. However, a first important use of the data presented in this paper is the estimation of the relative distance between the two MCs. In turn, the assumption of a distance for the LMC, which can be more safely determined with respect to the SMC's (since the SMC is so significantly elongated), allows us to provide an estimate of the absolute distance to the SMC (or, rather, of the center defined by the CC distribution).

We hence proceeded using our own data published in Ripepi et al. (2012a) for the CCs in the LMC. This is justified because (i) we used data in the same photometric system, (ii) we obtained a $PW(V, K_s)$ relation with very low dispersion for the LMC CCs, and (iii) we also provided an absolute distance estimate for the LMC.

²⁰ Note that Inno et al. (2013)'s $PW(V, K_s)$ relations are not provided for different breaks, nor do they have relations for $\log P > 0.45$

The technique adopted is illustrated in Fig. 20, where we compare the $PW(V, K_s)$ relations for F- and FO-mode pulsators (top and bottom panels, respectively). First, observing the period distribution of the CCs in the LMC and the fact that the slope of the LMC's $PW(V, K_s)$ relation is very close to the slope we have found here for the SMC CCs characterized by $\log P > 0.47$, we used this latter relation for our comparison of F-mode pulsators. Nonetheless, the slopes of the relations for both F- and FO-mode pulsators are slightly different for the LMC and SMC (which is possibly related to a weak but significant metallicity dependence). Indeed, it is possible to describe the difference in $W(V, K_s)$, which translates directly into a difference in distance modulus μ as a function of period with two simple equations:

$$\Delta\mu_F = (0.49 \pm 0.02) + (0.06 \pm 0.03) \log P \quad (10)$$

$$\Delta\mu_{FO} = (0.58 \pm 0.01) - (0.06 \pm 0.03) \log P \quad (11)$$

where $\Delta\mu$ means the difference in distance modulus of SMC and LMC, and the errors take into account the uncertainties in both the LMC and SMC relations. To use Eq. 10 and 11, we have to fix pivoting periods to determine the $\Delta\mu$ values. After some tests we chose $P = 10$ d and $P = 2$ d for F- and FO-mode pulsators, respectively. These values are approximately in the middle of the period range for both pulsator types, but it is easy to verify that the results do not depend significantly on this choice. The result of this exercise gives: $\Delta\mu_F = 0.55 \pm 0.04$ mag and $\Delta\mu_{FO} = 0.56 \pm 0.03$ mag, in excellent mutual agreement. Averaging the two results we obtain our best estimate for the relative distance between the MCs: $\Delta\mu = 0.55 \pm 0.04$ mag. This value is in good agreement with that derived in a similar fashion by Inno et al. (2013), especially with their result for FO pulsators: $\Delta\mu = 0.52 \pm 0.03$ mag, while for F-mode CCs they find $\Delta\mu = 0.48 \pm 0.03$ mag. Our estimate is somewhat larger than those quotes in other papers based on different standard candles (see de Grijs et al. 2014, for a large compilation of distance differentials). For example, Cioni et al. (2000b) found $\Delta\mu = 0.44 \pm 0.05$ from the tip of the red-giant branch, while using RR Lyrae stars Szewczyk et al. (2009) found a significantly smaller value, $\Delta\mu = 0.327 \pm 0.002$ mag. According to Matsunaga et al. (2011), Type II Cepheids (W Vir) yield $\Delta\mu = 0.40 \pm 0.07$ or $\Delta\mu = 0.39 \pm 0.05$ mag (depending on the use of NIR or optical data, respectively). In general, Table 4 of Matsunaga et al. (2011), where they list several literature results, seems to suggest that all evaluations of the $\Delta\mu$ based on CCs provide larger values with respect to those based on population II indicators. This can be due to the very different spatial distribution among CCs (typically showing a disk-like location in both MCs) and population II tracers (e.g., RR Lyrae stars, type II Cepheids, which are more evenly distributed around a sort of spheroid in both MCs), as shown, e.g., by Deb & Singh (2014); Moretti et al. (2014); Deb et al. (2015).

The absolute distance to the SMC can be determined by simply adding to the $\Delta\mu$ estimated above the preferred absolute distance for the LMC. There are hundreds of such estimates in the literature (see de Grijs et al. 2014, for a thorough review), but here we will consider in particular two values: (1) $\mu_{LMC} = 18.46 \pm 0.03$

mag obtained in our previous work on LMC CCs (Ripepi et al. 2012a), and (2) $\mu_{LMC} = 18.49 \pm 0.05$, accurately estimated by Pietrzyński et al. (2013) on the basis of an eclipsing Cepheid binary star. As a result, we obtain: (1) $\mu_{SMC} = 19.01 \pm 0.05$ mag and (2) $\mu_{SMC} = 19.04 \pm 0.06$ mag. These values are formally in agreement within $\sim 1\sigma$ with that obtained in de Grijs & Bono (2015) by averaging a large number of literature estimates: $\mu_{SMC} = 18.96 \pm 0.02$ mag. However, as noted by these latter authors, the systematic uncertainty on this determination, caused by different sources (mainly the complex SMC geometry and its elongation along the line of sight), can be as large as 0.15–0.20 mag.

6. CONCLUSIONS

In this paper we have presented the VMC survey's light curves for 4172 CCs in the SMC. The majority of the objects have optical V, I data as well as identification and periods from the OGLE III survey, while 13 CCs have been identified by the EROS 2 survey. Our data set consists of Y, J , and K_s light curves with the number of epochs typically ranging from 4 to 12 in Y and J , and 13 to 36 in K_s . We used our best light curves in each filter to construct samples of eight templates covering the full variety of periods and light-curve shapes. These templates have been used to automatically perform least-squares fits to the observations by varying both the amplitude and the phasing, and eventually choosing the best-fitting template by means of appropriately chosen parameters. We provide intensity-averaged magnitudes and peak-to-peak amplitudes in the Y, J , and K_s filters. To estimate reliable uncertainties on these values, we carried out Monte Carlo simulations, producing 100 mock light curves, adding Gaussian errors to the actual data for each CC in each filter, and running the template-fitting procedure from scratch each time. This process allowed us to assess the reliability of our template-fitting procedure and estimate robust uncertainties on CC magnitudes and amplitudes.

The intensity-averaged magnitudes in the VISTA Y, J , and K_s filters have been complemented with optical V -band data and periods to construct a variety of PL, PW , and PLC relations for the CCs in the SMC. The relations involving V, J , and K_s are in agreement with those in the literature. As for the Y band, to our knowledge in this paper we present the first CC PL, PW , and PLC ever obtained using this filter. The PL, PW , and PLC relations in the V, J , and K_s bands for F- and FO-mode CCs in the SMC presented here are the most accurate to date, since they are based on well- or moderately well-sampled light curves in K_s and J , respectively. We also presented the first NIR PL, PW , and PLC relations for SO pulsators to date.

We used the $PW(V, K_s)$ relation to estimate the relative SMC–LMC distance and, in turn, the absolute distance of the SMC. For the former, we derive $\Delta\mu = 0.55 \pm 0.04$ mag, a value that is in rather good agreement with other evaluations based on CCs, but in disagreement (significantly larger) with estimates based on (old) population II distance indicators. We speculate that this discrepancy may be mainly due to the different geometric distribution of young and old tracers in the MCs. As for the absolute distance to the SMC, our best estimates, $\mu_{SMC} = 19.01 \pm 0.05$ mag and $\mu_{SMC} = 19.04 \pm 0.06$

mag, based on two particular evaluations of the distance to the LMC, are in good agreement with literature values. However, we have to take into account the large systematic uncertainty due to the complex geometry of the SMC. In a forthcoming paper, we will use our precise PW relations to unveil the 3D structure of the SMC. For the reasons outlined above, this work is also expected to reduce the systematic uncertainties associated with the absolute distance to the SMC.

We thank our anonymous referee for his/her pertinent and helpful comments. This paper is based on observations taken with the ESO/VISTA telescope located at Paranal (Chile). V. R. warmly thanks Roberto Molinaro for providing the software for the spline interpolation and the Fourier analysis used to construct the template light curves. Partial financial support for this work was provided by PRIN MIUR 2011 (PI: F. Matteucci). We thank the UKs VISTA Data Flow System comprising the VISTA pipeline at CASU and the VISTA Science Archive at Wide Field Astronomy Unit (Edinburgh; WFAU) for providing calibrated data products supported by the STFC. This work was partially supported by the Gaia Research for European Astronomy Training (GREAT-ITN) Marie Curie network, funded through the European Union Seventh Framework Programme ([FP7/2007-1312 2013] under grant agreement no. 264895). M.-R. L. C. acknowledges support from the German Exchange service. This work is supported by STFC grants ST/5001333 and ST/M001008. R. d. G. acknowledges financial support from the National Natural Research Foundation of China (grant 11373010).

REFERENCES

- Bessell, M. S., & Brett, J. M. 1988, *PASP*, 100, 1134
 Bono, G., Caputo, F., Castellani, V., & Marconi, M. 1999, *ApJ*, 512, 711
 Bono, G., Castellani, V., & Marconi, M. 2000, *ApJ*, 529, 293
 Bono, G., Caputo, F., & Marconi, M. 2001a, *MNRAS*, 325, 1353
 Bono, G., Gieren, W. P., Marconi, M., & Fouqué, P. 2001b, *ApJL*, 552, L141
 Bono, G., Caputo, F., Marconi, M., & Musella, I. 2010, *ApJ*, 715, 277
 Caputo, F., Marconi, M., & Musella, I. 2000, *A&A*, 354, 610
 Carpenter, J. M. 2001, *AJ*, 121, 2851
 Cardelli, J. A., Clayton, G. C., & Mathis, J. S. 1989, *ApJ*, 345, 245
 Carini, R., Brocato, E., Marconi, M., & Raimondo, G. 2014, *A&A*, 561, A110
 Cioni, M.-R. L., Habing, H. J., & Israel, F. P. 2000a, *A&A*, 358, L9
 Cioni, M.-R. L., van der Marel, R. P., Loup, C., & Habing, H. J. 2000b, *A&A*, 359, 601
 Cioni, M.-R. L., Clementini, G., Girardi, L., et al. 2011, *A&A*, 527, A116
 Cross, N. J. G., et al. 2012, *A&A*, 548, A119
 Dalton, G. B., Caldwell, M., Ward, A. K., et al. 2006, *Proc. SPIE*, 6269, 62690X
 Deb, S., Singh, H. P., Kumar, S., & Kanbur, S. M. 2015, *MNRAS*, 449, 2768
 Deb, S., & Singh, H. P. 2014, *MNRAS*, 438, 2440
 Fiorentino, G., Musella, I., & Marconi, M. 2013, *MNRAS*, 434, 2866
 de Grijs, R., Wicker, J. E., & Bono, G. 2014, *AJ*, 147, 122
 de Grijs, R., & Bono, G. 2015, *AJ*, 149, 179
 Deb, S., Singh, H. P., Kumar, S., & Kanbur, S. M. 2015, *MNRAS*, 449, 2768
 Dobbie, P. D., Cole, A. A., Subramaniam, A., & Keller, S. 2014, *MNRAS*, 442, 1663
 Emerson J. P., Irwin M. J., Lewis J., et al., 2004, *Proc. SPIE*, 5493, 401, 41
 Emerson, J., McPherson, A., & Sutherland, W. 2006, *The Messenger*, 126, 41
 Fiorentino, G., Caputo, F., Marconi, M., & Musella, I. 2002, *ApJ*, 576, 402
 Freedman, W. L. 1988, *ApJ*, 326, 691
 Freedman, W. L., Madore, B. F., Gibson, B. K., et al. 2001, *ApJ*, 553, 47
 Freedman W. L., Madore B. F., 2011, *ApJ*, 734, 46
 Gao, J., Jiang, B. W., Li, A., & Xue, M. Y. 2013, *ApJ*, 776, 7
 Glatt, K., Grebel, E. K., Sabbi, E., et al. 2008, *AJ*, 136, 1703
 Hammer, F., Yang, Y. B., Flores, H., Puech, M., & Fouquet, S. 2015, *ApJ*, 813, 110
 Harris, 2007, *ApJ*, 658, 345
 Harris J., Zaritsky D., 2004, *AJ*, 127, 1531
 Harris J., Zaritsky, D., 2009, *AJ*, 138, 1243
 Haschke R., Grebel E. K., Duffau, S., 2011, *AJ*, 141, 158
 Haschke, R., Grebel, E. K., & Duffau, S. 2012, *AJ*, 144, 107
 Hatzidimitriou, D., & Hawkins, M. R. S. 1989, *MNRAS*, 241, 667
 Inno, L., Matsunaga, N., Bono, G., et al. 2013, *ApJ*, 764, 84
 Inno, L., Matsunaga, N., Romaniello, M., et al. 2015, *A&A*, 576, A30
 Irwin, M. J., Kunkel, W. E., & Demers, S. 1985, *Nature*, 318, 160
 Irwin M. J., Lewis J., Hodgkin S., et al., 2004, *Proc. SPIE*, 5493, 411
 Irwin, M. J. 2009, *UKIRT Newsletter*, 25, 15
 Kerber L. O., Girardi L., Rubele S., Cioni M.-R., 2009, *A&A*, 499, 697
 Kim, D.-W., Protopapas, P., Bailer-Jones, C. A. L., et al. 2014, *A&A*, 566, A43
 Macri, L. M., Ngeow, C.-C., Kanbur, S. M., Mahzooni, S., & Smitka, M. T. 2015, *AJ*, 149, 117
 Madore, B. F. 1982, *ApJ*, 253, 575
 Marconi, M., Fiorentino, G., & Caputo, F. 2004, *A&A*, 417, 1101
 Marconi, M., Musella, I., & Fiorentino, G. 2005, *ApJ*, 632, 590
 Marconi, M. 2009, *Mem. Soc. Astron. Italiana*, 80, 141
 Marconi, M., Musella, I., Fiorentino, G., et al. 2010, *ApJ*, 713, 615
 Matsunaga, N., Feast, M. W., & Soszyński, I. 2011, *MNRAS*, 413, 223
 Moretti, M. I., Clementini, G., Muraveva, T., et al. 2014, *MNRAS*, 437, 2702
 Muraveva, T., Palmer, M., Clementini, G., et al. 2015, *ApJ*, 807, 127
 Nidever, D. L., Monachesi, A., Bell, E. F., et al. 2013, *ApJ*, 779, 145
 Ngeow, C., Kanbur, S. M., & Nanthakumar, A. 2008, *A&A*, 477, 621
 Persson S. E., Madore B. F., Krzemiński W., et al., 2004, *AJ*, 128, 2239
 Piatti, A. E., de Grijs, R., Rubele, S., et al. 2015, *MNRAS*, 450, 552
 Pietrzyński, G., Graczyk, D., Gieren, W., et al. 2013, *Nature*, 495, 76
 Putman, M. E., Gibson, B. K., Staveley-Smith, L., et al. 1998, *Nature*, 394, 752
 Riess, A. G., Macri, L., Casertano, S., et al. 2011, *ApJ*, 730, 119
 Ripepi, V., Moretti, M. I., Marconi, M., et al. 2012a, *MNRAS*, 424, 1807
 Ripepi, V., Moretti, M. I., Clementini, G., et al. 2012b, *Ap&SS*, 341, 51
 Ripepi, V., Cignoni, M., Tosi, M., et al. 2014, *MNRAS*, 442, 1897
 Ripepi, V., Marconi, M., Moretti, M. I., et al. 2014, *MNRAS*, 437, 2307
 Ripepi, V., Moretti, M. I., Marconi, M., et al. 2015, *MNRAS*, 446, 3034
 Romaniello, M., Primas, F., Mottini, M., et al. 2008, *A&A*, 488, 731
 Rubele, S., Girardi, L., Kerber, L., et al. 2015, *MNRAS*, 449, 639
 Scowcroft, V., Freedman, W. L., Madore, B. F., et al. 2016, *ApJ*, 816, 49
 Shapley H., 1940, *Bull. Harvard Coll. Obs.*, 914, 8
 Schaltenbrand, R., & Tammann, G. A. 1971, *A&AS*, 4, 265
 Skrutskie, M. F., Cutri, R. M., Stiening, R., et al. 2006, *AJ*, 131, 1163
 Soszyński, I., Gieren, W., & Pietrzyński, G. 2005, *PASP*, 117, 823

Soszyński, I., Poleski, R., Udalski, A., et al. 2010, *Acta Astronomica*, 60, 17
 Stanimirović, S., Staveley-Smith, L., & Jones, P. A. 2004, *ApJ*, 604, 176
 Subramanian, S., & Subramanian, A. 2015, *A&A*, 573, A135
 Szewczyk, O., Pietrzyński, G., Gieren, W., et al. 2009, *AJ*, 138, 1661
 Tisserand, P., Le Guillou, L., Afonso, C., et al. 2007, *A&A*, 469, 387

Udalski, A., Szymanski, M., Kubiak, M., et al. 1999, *Acta Astronomica*, 49, 201
 Welch, D. L., McLaren, R. A., Madore, B. F., & McAlary, C. W. 1987, *ApJ*, 321, 162
 Westerlund B. E., 1997, *The Magellanic Clouds*. CUP, Cambridge
 Zaritsky, D., Harris, J., Grebel, E. K., & Thompson, I. B. 2000, *ApJL*, 534, L53

Table 1
Number of CCs in each VMC SMC tile.

Tile	RA			DEC			N
	hh	mm	ss.sss	°	'	"	
SMC 3.3	00	44	55.896	-74	12	42.120	315
SMC 3.5	01	27	30.816	-74	00	49.320	25
SMC 4.2	00	25	14.088	-73	01	47.640	86
SMC 4.3	00	45	14.688	-73	07	11.280	1642
SMC 4.4	01	05	19.272	-73	05	15.360	1128
SMC 4.5	01	25	11.088	-72	56	02.760	83
SMC 5.2	00	26	41.688	-71	56	35.880	2
SMC 5.3	00	45	32.232	-72	01	40.080	197
SMC 5.4	01	04	26.112	-71	59	51.000	687
SMC 6.3	00	45	48.792	-70	56	09.240	4
SMC 6.5	01	21	22.560	-70	46	11.640	3

Table 2
Number of CCs for each different mode of pulsation.

F	FO	SO	F/FO	FO/SO	F/FO/SO	FO/SO/TO
2377	1472	74	52	196	2	1

Table 3
 Y , J and K_s time series photometry for the CCs investigated in this paper. The data below refer to the variable OGLE-SMC-CEP-2476.

$HJD - 2400000$	Y	σ_Y
55492.59731	19.076	0.040
55492.63328	19.130	0.040
55497.70319	19.116	0.047
55539.61969	19.114	0.051
$HJD - 2400000$	J	σ_J
55493.58975	18.788	0.041
55493.62870	18.830	0.039
55495.55177	18.860	0.063
55539.64087	18.912	0.060
55778.75378	18.817	0.052
$HJD - 2400000$	K_s	σ_{K_s}
55493.78892	18.641	0.099
55495.57575	18.699	0.168
55495.68566	18.688	0.111
55497.72461	18.776	0.153
55538.62081	18.681	0.125
55549.58532	18.777	0.135
55769.75425	18.697	0.126
55778.77517	18.683	0.169
55791.76203	18.706	0.110
55818.73171	18.807	0.148
55820.67458	18.484	0.088
55879.55553	18.542	0.111
55880.61929	18.737	0.137
55900.57090	18.674	0.115
56130.79475	18.704	0.116
56173.70295	18.712	0.136
56195.64097	18.668	0.111
56223.54177	18.704	0.125

Note. — Table 3 is published in its entirety in the electronic edition of the *Astrophysical Journal*. A portion is shown here for guidance regarding its form and content.

Table 4

Fourier parameters adopted to construct the templates in the VISTA Y, J, K_s bands.
 Note that the template starts from 2 because template 1 (T1) is a simple cosine function.

Parameter	T2	T3	T4	T5	T6	T7	T8
Y-Band							
a_1	0.49260	0.12614	0.12888	0.20863	0.20097	0.17442	0.15502
a_2	0.14500	0.03315	0.07549	0.11718	0.09804	0.05488	0.03855
a_3	0.04100	0.01090	0.04152	0.05601	0.04747	0.02273	0.02314
a_4	0.01000	0.00448	0.01609	0.02200	0.01831	0.01211	0.00984
a_5	0.00000	0.00209	0.00580	0.00765	0.00370	0.00640	0.00483
a_6	0.00000	0.00124	0.00000	0.00253	0.00190	0.00345	0.00146
a_7	0.00000	0.00065	0.00000	0.00026	0.00276	0.00171	0.00078
a_8	0.00000	0.00035	0.00000	0.00044	0.00173	0.00081	0.00054
a_9	0.00000	0.00022	0.00000	0.00008	0.00054	0.00031	0.00041
a_{10}	0.00000	0.00017	0.00000	0.00027	0.00024	0.00010	0.00022
ϕ_1	1.40800	5.75860	2.52701	1.50221	0.72710	5.27327	5.93367
ϕ_2	2.52800	3.65703	3.36472	1.50458	6.08919	3.02993	4.57391
ϕ_3	3.55200	1.23267	4.18291	1.34113	5.11517	1.14020	3.82891
ϕ_4	4.43800	5.38378	5.03844	0.97634	4.16420	5.46810	1.84753
ϕ_5	0.00000	3.36130	5.72830	0.30153	3.35092	3.52010	1.18378
ϕ_6	0.00000	1.20985	0.00000	5.90041	5.31224	1.54636	4.81460
ϕ_7	0.00000	5.24591	0.00000	0.00420	4.58734	5.86030	5.81304
ϕ_8	0.00000	3.03051	0.00000	1.40454	3.82023	3.83808	0.48183
ϕ_9	0.00000	1.01212	0.00000	0.34470	3.26788	1.67678	3.77426
ϕ_{10}	0.00000	5.12881	0.00000	3.91317	4.72011	5.36878	4.02321
J-Band							
a_1	0.49260	0.10773	0.12934	0.10873	0.12532	0.12790	0.15502
a_2	0.14500	0.01461	0.06480	0.04565	0.03672	0.05709	0.03855
a_3	0.04100	0.02933	0.03052	0.02487	0.00939	0.00983	0.02314
a_4	0.01000	0.00196	0.01328	0.00825	0.00303	0.00215	0.00984
a_5	0.00000	0.00177	0.00547	0.00220	0.00170	0.00151	0.00483
a_6	0.00000	0.00010	0.00254	0.00091	0.00020	0.00072	0.00146
a_7	0.00000	0.00013	0.00135	0.00018	0.00012	0.00021	0.00078
a_8	0.00000	0.00011	0.00061	0.00057	0.00040	0.00002	0.00054
a_9	0.00000	0.00004	0.00023	0.00046	0.00023	0.00003	0.00041
a_{10}	0.00000	0.00004	0.00019	0.00031	0.00024	0.00006	0.00022
ϕ_1	1.40800	0.22905	2.72672	5.39342	1.09258	5.12094	5.93367
ϕ_2	2.52800	4.86405	4.06800	3.37087	0.70885	2.95240	4.57391
ϕ_3	3.55200	3.12523	5.42088	1.47564	0.70180	0.78702	3.82891
ϕ_4	4.43800	1.79845	0.59352	5.60246	1.22024	5.53095	1.84753
ϕ_5	0.00000	1.00316	2.17713	2.89183	1.40527	2.77300	1.18378
ϕ_6	0.00000	5.97019	3.76033	0.28963	0.69902	0.39488	4.81460
ϕ_7	0.00000	5.69884	5.19037	0.47083	5.83421	5.20192	5.81304
ϕ_8	0.00000	5.29476	0.22745	5.03774	5.32133	3.10882	0.48183
ϕ_9	0.00000	2.24848	1.14384	2.56761	5.91469	2.69578	3.77426
ϕ_{10}	0.00000	2.92779	2.44216	6.20944	5.71899	5.71612	4.02321
K_s -Band							
a_1	0.49260	0.11057	0.18142	0.10520	0.15750	0.10319	0.10789
a_2	0.14500	0.04102	0.02969	0.03653	0.02199	0.03305	0.04682
a_3	0.04100	0.01533	0.00711	0.01983	0.00921	0.01029	0.02355
a_4	0.01000	0.00440	0.00214	0.01085	0.00367	0.00155	0.01431
a_5	0.00000	0.00089	0.00302	0.00550	0.00224	0.00001	0.00800
a_6	0.00000	0.00078	0.00146	0.00259	0.00119	0.00011	0.00448
a_7	0.00000	0.00048	0.00051	0.00127	0.00064	0.00032	0.00232
a_8	0.00000	0.00004	0.00069	0.00079	0.00036	0.00033	0.00088
a_9	0.00000	0.00016	0.00016	0.00058	0.00028	0.00018	0.00028
a_{10}	0.00000	0.00014	0.00049	0.00045	0.00021	0.00000	0.00000
ϕ_1	1.40800	1.27522	1.10728	1.31803	1.57541	4.75055	1.48634
ϕ_2	2.52800	1.80953	2.41492	2.06525	2.75238	2.11317	2.14552
ϕ_3	3.55200	2.46781	2.77198	2.84018	4.16989	5.38840	2.71326
ϕ_4	4.43800	2.94883	2.45223	3.61468	5.36458	2.83264	3.39001
ϕ_5	0.00000	2.46814	2.58196	4.34756	0.48850	4.55134	3.97662
ϕ_6	0.00000	1.69940	3.83981	4.99929	2.10232	1.60734	4.48671
ϕ_7	0.00000	2.00844	2.89989	5.50476	3.90737	5.88377	5.06340
ϕ_8	0.00000	2.26548	4.29762	5.96834	5.73100	3.05768	5.44150
ϕ_9	0.00000	6.16960	3.43667	0.23028	1.22432	0.08505	5.61231
ϕ_{10}	0.00000	0.16239	4.88214	0.80864	2.94561	4.77334	0.00000

Table 5

Results of the template-fitting procedure. Columns: (1) Identification from OGLE:III (OGLE-SMC-CEP- plus the numbers listed below) or EROS 2; (2) VMC tile in which the object is found; (3) Right Ascension; (4) Declination; (5) Mode: F=Fundamental; FO=First Overtone; SO=Second overtone; TO=Third Overtone; (6) Period; (7) Number of epochs in Y ; (8)–(9) Intensity-averaged magnitude in Y and relative uncertainty; (10)–(11) Peak-to-peak amplitude in Y and relative uncertainty; (12) to (16) As for column (7) to (11) but for the J band; (17) to (21) As for column (7) to (11) but for the K_s band; (22) Flag assigned using the $PW(V, K_s)$ as reference relation: 0=no remark; 1=overluminous star with separation between VMC and OGLE:III position larger than 0.2 arcsec; 2=largely scattered or under-sampled light curve; 3=Remarks OGLE:III; 4= Remarks VMC; 5=Saturation; 10–11=F- or FO-mode outliers without evident explanation; 12=V band lacking. The first part of the table includes all stars with flag = 0 ordered by increasing period; the second part includes all stars with flag>0, sorted by increasing period. The sorting of the table is the same as in Figs 10, 11, and 12. We show the first 20 rows of the table to indicate its form and content.

ID	Tile	RA deg	DEC deg	Mode	Period d	n_Y	Y mag	$\sigma(Y)$ mag	$A(Y)$ mag	$\sigma A(Y)$ mag	n_J	J mag	$\sigma(J)$ mag	$A(J)$ mag	$\sigma A(J)$ mag	n_{K_s}	K_s mag	$\sigma(K_s)$ mag	$A(K_s)$ mag	$\sigma A(K_s)$ mag	Flag
1	2	3	4	5	6	7	8	9	10	11	12	13	14	15	16	17	18	19	20	21	22
2476	5.4	13.991833	-72.442611	FO/SO	0.252601	4	19.058	0.087	0.10	0.09	5	18.873	0.056	0.15	0.09	18	18.696	0.057	0.110	0.085	0
3867	4.4	16.676208	-73.416917	FO/SO/TO	0.268847	4	18.454	0.026	0.19	0.04	5	18.245	0.029	0.15	0.06	14	18.041	0.036	0.050	0.052	0
2507	4.4	14.038583	-73.251389	FO/SO	0.277552	4	18.645	0.026	0.11	0.05	5	18.422	0.004	0.10	0.01	14	18.213	0.065	0.184	0.092	0
0022	4.2	5.892208	-73.399694	FO	0.313664	5	18.442	0.004	0.17	0.01	5	18.268	0.021	0.10	0.03	14	18.061	0.035	0.087	0.064	0
1471	5.3	12.571750	-72.043333	FO/SO	0.327181	5	17.736	0.014	0.07	0.02	9	17.550	0.010	0.11	0.02	16	17.326	0.017	0.065	0.019	0
3287	4.4	15.427042	-73.294194	FO	0.346422	4	18.061	0.014	0.14	0.04	5	17.878	0.015	0.11	0.03	14	17.676	0.027	0.126	0.037	0
1606	4.3	12.773167	-73.377056	FO/SO	0.352508	6	18.313	0.021	0.20	0.05	6	18.074	0.004	0.11	0.01	16	17.784	0.031	0.070	0.035	0
3784	4.4	16.470875	-72.891500	FO	0.380368	4	18.322	0.055	0.15	0.05	5	18.009	0.017	0.18	0.04	14	17.765	0.028	0.087	0.035	0
4243	4.4	17.760458	-73.161833	FO	0.393727	4	18.131	0.013	0.28	0.03	5	17.907	0.010	0.16	0.03	14	17.643	0.036	0.071	0.054	0
0310	4.3	9.822625	-73.240444	FO	0.394238	6	17.899	0.017	0.19	0.05	6	17.696	0.016	0.16	0.03	16	17.540	0.021	0.146	0.040	0
1357	4.3	12.404083	-73.025194	SO	0.401286	6	17.693	0.010	0.05	0.01	6	17.460	0.012	0.03	0.02	16	17.255	0.017	0.043	0.026	0
2265	3.3	13.668625	-73.801333	FO	0.408552	7	17.828	0.019	0.12	0.05	6	17.692	0.018	0.21	0.03	18	17.512	0.015	0.103	0.030	0
4465	4.5	18.738000	-72.666972	FO	0.421663	5	17.868	0.010	0.19	0.04	6	17.691	0.009	0.15	0.02	18	17.472	0.017	0.103	0.028	0
0358	4.3	10.121583	-73.447056	SO	0.442236	6	17.205	0.007	0.05	0.02	6	17.057	0.009	0.03	0.02	16	16.912	0.010	0.020	0.016	0
2290	3.3	13.713833	-73.872278	FO	0.444418	7	18.045	0.012	0.23	0.03	7	17.853	0.015	0.17	0.03	18	17.564	0.019	0.128	0.031	0
4618	4.5	20.858250	-72.729806	SO	0.445367	5	17.100	0.005	0.05	0.01	6	16.952	0.005	0.03	0.01	18	16.746	0.014	0.030	0.020	0
1085	4.3	12.000917	-72.865417	SO	0.452269	6	17.332	0.010	0.05	0.01	6	17.155	0.013	0.07	0.02	16	17.060	0.016	0.026	0.018	0
4096	5.4	17.286083	-72.275361	FO	0.487218	4	17.988	0.050	0.47	0.06	5	17.700	0.005	0.18	0.02	18	17.469	0.021	0.110	0.034	0
2907	4.4	14.730208	-73.550722	FO/SO	0.490294	4	17.607	0.048	0.22	0.05	5	17.540	0.016	0.21	0.03	14	17.274	0.019	0.080	0.031	0
1133	3.3	12.061292	-73.718278	SO	0.490791	13	17.253	0.006	0.02	0.01	13	17.063	0.007	0.01	0.01	34	16.905	0.009	0.014	0.010	0

Note. — Table 5 is published in its entirety in the electronic edition of the *Astrophysical Journal*. A portion is shown here for guidance regarding its form and content.

Table 6
PL, *PW*, and *PLC* relations for F and FO CCs. The Wesenheit functions are defined in the table.

Mode	α	σ_α	β	σ_β	γ	σ_γ	r.m.s.
$Y^0 = \alpha + \beta \log P$							
F $\log P < 0.47$	17.247	0.011	-3.413	0.043	0.196
F $\log P \geq 0.47$	17.016	0.024	-2.984	0.030	0.197
FO	16.605	0.006	-3.365	0.025	0.202
SO	15.91	0.06	-4.06	0.27	0.15
$J^0 = \alpha + \beta \log P$							
F $\log P < 0.47$	16.978	0.010	-3.469	0.040	0.182
F $\log P \geq 0.47$	16.763	0.021	-3.047	0.027	0.177
FO	16.372	0.005	-3.416	0.023	0.185
SO	15.73	0.06	-4.07	0.26	0.15
$K_s^0 = \alpha + \beta \log P$							
F $\log P < 0.47$	16.711	0.009	-3.578	0.036	0.166
F $\log P \geq 0.47$	16.513	0.019	-3.195	0.024	0.156
FO	16.133	0.005	-3.544	0.020	0.169
SO	15.52	0.06	-4.28	0.26	0.15
$W(Y, K_s) = K_s - 0.42(Y - K_s) = \alpha + \beta \log P$							
F $\log P < 0.47$	16.489	0.009	-3.660	0.035	0.158
F $\log P \geq 0.47$	16.301	0.017	-3.283	0.022	0.145
FO	15.933	0.005	-3.614	0.020	0.161
SO	15.37	0.06	-4.29	0.26	0.14
$W(J, K_s) = K_s - 0.69(J - K_s) = \alpha + \beta \log P$							
F $\log P < 0.47$	16.535	0.009	-3.685	0.034	0.153
F $\log P \geq 0.47$	16.343	0.017	-3.301	0.021	0.139
FO	15.964	0.005	-3.618	0.019	0.156
SO	15.39	0.06	-4.31	0.26	0.15
$W(V, K_s) = K_s - 0.13(V - K_s) = \alpha + \beta \log P$							
F $\log P < 0.47$	16.559	0.008	-3.666	0.033	0.147
F $\log P \geq 0.47$	16.360	0.016	-3.265	0.021	0.137
FO	15.984	0.004	-3.591	0.019	0.154
SO	15.40	0.06	-4.28	0.26	0.15
$K_s^0 = \alpha + \beta \log P + \gamma(Y - K_s)_0$							
F $\log P < 0.47$	16.619	0.020	-3.608	0.036	0.17	0.03	0.164
F $\log P \geq 0.47$	16.239	0.035	-3.312	0.026	0.55	0.06	0.146
FO	15.923	0.023	-3.629	0.021	0.44	0.05	0.163
SO	15.62	0.10	-4.21	0.28	-0.25	0.19	0.16
$K_s^0 = \alpha + \beta \log P + \gamma(J - K_s)_0$							
F $\log P < 0.47$	16.535	0.022	-3.649	0.036	0.66	0.07	0.161
F $\log P \geq 0.47$	16.227	0.032	-3.372	0.028	1.16	0.11	0.144
FO	15.911	0.021	-3.657	0.021	0.92	0.08	0.162
SO	15.64	0.08	-4.23	0.27	-0.65	0.30	0.16
$K_s^0 = \alpha + \beta \log P + \gamma(V - K_s)_0$							
F $\log P < 0.47$	16.164	0.031	-3.776	0.033	0.445	0.024	0.145
F $\log P \geq 0.47$	15.879	0.035	-3.498	0.024	0.543	0.027	0.121
FO	15.676	0.025	-3.710	0.020	0.402	0.022	0.149
SO	15.39	0.12	-4.28	0.26	0.14	0.12	0.15